

1  
2  
3  
4  
5  
6  
7  
8  
9  
10  
11  
12  
13  
14  
15  
16  
17  
18  
19  
20  
21  
22  
23

**Chemical and physical erosion rhythms of the West African Cenozoic  
morphogenesis:  $^{39}\text{Ar}$ - $^{40}\text{Ar}$  dating of supergene K-Mn oxides**

Anicet Beauvais <sup>a\*</sup>, Gilles Ruffet <sup>b</sup>, Olivier Hénocque <sup>a</sup>, Fabrice Colin <sup>c</sup>

<sup>a</sup> *CEREGE (Centre Européen de Recherche et d'Enseignement de Géosciences de  
l'Environnement), Aix-Marseille Université, CNRS, IRD, CdF, BP 80, 13545 Aix-en-  
Provence Cedex 4, France*

<sup>b</sup> *Géosciences Rennes, Université de Rennes 1, CNRS, CAREN, 35042 Rennes Cedex, France*

<sup>c</sup> *IRD (Institut de Recherche pour le Développement), BP A5, 98848 Nouméa, Nouvelle-  
Calédonie*

\* Corresponding author: [beauvais@cerege.fr](mailto:beauvais@cerege.fr) (Tel/Fax: 33 4 42 97 17 73/ 33 4 42 97 15 95)

24 **Abstract**

25  
26 Chemical weathering and mechanical erosion are first order processes of long-term  
27 tropical morphogenesis, which is still poorly deciphered for lack of time constraints. We  
28 address this issue by laser-probe  $^{39}\text{Ar}$ - $^{40}\text{Ar}$  dating of generations of cryptomelane [ $\text{K}_1$ -  
29  ${}_2\text{Mn}_8\text{O}_{16}, n\text{H}_2\text{O}$ ] from the manganese ore deposit of Tambao in northern Burkina Faso. This  
30 Mn deposit results from the supergene weathering of carbonate and silicate Mn-protores  
31 underneath lateritic palaeolandsurfaces. It consists of an upper cryptomelane-rich domain, and  
32 a lower domain where pyrolusite ( $\beta\text{-MnO}_2$ ) is the dominant Mn-oxide. The oldest  $^{39}\text{Ar}$ - $^{40}\text{Ar}$   
33 ages (59-45 Ma) are obtained on surface outcrops while the youngest ones characterize deep  
34 oxidation fronts (3.4-2.9 Ma). Apparent correlations of  $^{39}\text{Ar}$ - $^{40}\text{Ar}$  age groups with  $\delta^{18}\text{O}$  and  
35 eustatic curves allow definition of the different stages of morphogenesis. Paleocene-Eocene  
36 ages (59-45 Ma), bracket a greenhouse period propitious to bauxitic weathering. The lack of  
37 significant ages between ca. 45 Ma and 29 Ma characterizes a period dominated by  
38 mechanical erosion, during which detrital sediments including lateritic materials were  
39 accumulated in intracratonic basins allowing the exhumation of a new lateritic landsurface.  
40 Two major weathering periods separated by a second erosion episode (24-18 Ma) are also  
41 depicted at the end of Oligocene (29-24 Ma) and lower to mid-Miocene (18-11.5 Ma) in the  
42 upper domain, during which newly shaped landsurfaces conspicuously weathered. The shorter  
43 weathering and erosion episodes recorded in the lower domain from ca 18 Ma to ca 2.9 Ma  
44 led to the final geomorphic changes that were conducive to the formation of glacis. The  
45 preservation of old cryptomelane (59-45 Ma) in the upper part of the ore deposit indicates a  
46 Cenozoic denudation limited to the erosion of previous bauxites, and partly, of ferricretes.

47  
48 *Keywords* – Laser-probe  $^{39}\text{Ar}$ - $^{40}\text{Ar}$  dating, Cryptomelane, Lateritic paleolandsurface,

49 Cenozoic denudation, Long-term morphogenesis, West Africa

50

## 50 **1. Introduction**

51  
52 Most lateritic deposits and tropical soils result from long-term meteoric weathering of the  
53 lithosphere and are still widespread on the Earth surface, especially throughout the tropical  
54 belt [*Pedro*, 1968; *Nahon*, 1991]. Following Gondwana break-up, physical and chemical  
55 processes driven by epeirogeny and climate led to the development of tens of meters of thick  
56 weathering mantles including bauxites and ferricretes, which are preserved on stepped relicts  
57 of abandoned planation surfaces and pediplains [*Millot*, 1983; *Aleva*, 1984; *Bardossy and*  
58 *Aleva*, 1990; *Nahon et al.*, 1992; *Tardy and Roquin*, 1998; *Chevillotte et al.*, 2006]. These  
59 lateritic paleosurface relicts result from the combination of long-term weathering, incision  
60 and erosion processes [*King*, 1967; *Partridge and Maud*, 1987]. According to the synthetic  
61 morphogenetic sequence described in West Africa [*Vogt*, 1959; *Michel*, 1973; *Grandin*, 1976;  
62 *Boulangé and Millot*, 1988; *Thomas*, 1994], the highest surfaces carrying bauxite dominate  
63 landsurfaces with different generations of ferricrete (Figure 1). Manganese ore deposits may  
64 also develop within specific rock's weathering mantles. Below the bauxitic paleosurface, the  
65 intermediate ferricrete-capped relief dominates three pediments (Figure 1) so called lateritic  
66 glacis in West Africa [*Thomas*, 1994], and defined as high, middle and low glacis. The term  
67 glacis defines a gently inclined surface carrying detrital lateritic and bedrock materials.

68 The age determination of the paleosurfaces and their lateritic weathering remains a  
69 critical issue in estimating the erosion rates and constraining the long-term tropical  
70 morphogenesis and the evolution of continental palaeoclimates. A relative chronology of the  
71 lateritic landsurfaces was assessed by examining the height differences between the  
72 landsurfaces and the geochemical composition of the associated lateritic materials that  
73 allowed a first estimation of the erosion rates [*Tardy and Roquin*, 1998]. However, better-  
74 constrained ages of past chemical weathering and mechanical erosion periods can be obtained  
75 by performing  $^{39}\text{Ar}$ - $^{40}\text{Ar}$  laser-probe dating of K-Mn oxides in supergene manganese ore

76 deposits that constitute a perfect alternative to the apatite fission track approach [Gunnell,  
77 2003] to constrain the Cenozoic cratonic denudation for different time spans.

78 Previous geochronological studies proved the usefulness of K-Ar and  $^{39}\text{Ar}$ - $^{40}\text{Ar}$  methods  
79 to date potassium-rich supergene minerals such as cryptomelane [Vasconcelos *et al.*, 1992,  
80 1994; Lippolt and Hautmann, 1995; Ruffet *et al.*, 1996; Hénocque *et al.*, 1998]. This K-Mn  
81 oxide is believed to reflect strong lateritic weathering conditions [Parc *et al.*, 1989], and it is  
82 ubiquitous in numerous supergene manganese ore deposits [Nahon *et al.*, 1984; Beauvais *et*  
83 *al.*, 1987; Roy, 1981, 1988; Dasgupta *et al.*, 1992; Ostwald, 1992; Pracejus and Bolton, 1992;  
84 Varentsov, 1996]. The Tambao Mn ore deposit in northern Burkina Faso is clearly integrated  
85 in the continental scale geomorphological sequence (Figure 1) and its high cryptomelane  
86 content [Perseil and Grandin, 1978] motivated  $^{39}\text{Ar}$ - $^{40}\text{Ar}$  geochronological investigations.  
87  $^{39}\text{Ar}$ - $^{40}\text{Ar}$ -laser method was first performed on two Mn-rich botryoidal concretions [Henocque  
88 *et al.*, 1998] that showed an episode of cryptomelane formation between 44.5 and 50 Ma.  
89 Later,  $^{39}\text{Ar}$ - $^{40}\text{Ar}$  age groups of 59-56 Ma, 47-44 Ma and 27-24 Ma were obtained on seven  
90 samples of manganiferous pisolites deriving from a massive Mn-crust [Colin *et al.*, 2005].  
91 These previous results allowed linking of the formation of surface Mn-crusts and pisolites to  
92 the Paleogene bauxitic period. In this paper we investigate many more samples from drill  
93 cores to better characterize the successive stages of the Mn-ore deposit formation that may  
94 usefully document the long-term (Paleogene + Neogene) morphogenesis and denudation.

95

## 96 **2. Material, sampling and analytical methods**

97

98 Cryptomelane occurs in single or multiple generations associated with other Mn-oxides  
99 [Beauvais *et al.*, 1987]. This is the K-rich end member of the hollandite Mn-oxide group with  
100 a general formula,  $\text{A}_{1-2}\text{B}_8\text{O}_{16} \cdot n\text{H}_2\text{O}$  (with  $\text{A} = \text{K}^+, \text{Ba}^{2+}, \text{Na}^+, \text{Pb}^{2+}$  and  $\text{B} = \text{Mn}^{4+}, \text{Mn}^{2+}, \text{Fe}^{3+},$   
101  $\text{Al}^{3+}$ ), and a tunnel structure made by double chains of  $\text{MnO}_6$  octahedra [Burns and Burns,

102 1979; *Turner and Buseck*, 1979]. Large cations of the A site counterbalance the charge deficit  
103 due to the Mn oxidation states and the other cations of the B site. The cryptomelane structure  
104 increases its potassium and argon retentiveness, and thus its suitability for K-Ar and  $^{39}\text{Ar}$ - $^{40}\text{Ar}$   
105 geochronological investigations [*Vasconcelos et al.*, 1992, 1994].

106 The first applications of the K-Ar dating method to cryptomelane were very promising  
107 despite problems of phase mixing and difficulties for extracting pure samples [*Chukhrov et*  
108 *al.*, 1966; *Yashvili and Gukasyan*, 1974; *Varentsov and Golovin*, 1987; *Segev et al.*, 1991].  
109 The small quantities required for  $^{39}\text{Ar}$ - $^{40}\text{Ar}$ -laser-probe dating reduce the mixing risks [*Ruffet*  
110 *et al.*, 1996], which are further lessened by a precise sampling [*Hénoque et al.*, 1998].

111

## 112 **2.1. Petrography and mineralogy**

113

114 Samples were taken from drill cores DD2B, DDH76-02 and DDH76-09 of 110-meter and  
115 40-meter-length, respectively (Figures 2 and 3) and from outcrops of manganese oxide  
116 benches. DD2B, DDH76-02 and DDH76-09 cores were drilled on the high and low hills  
117 (Figure 2). The altitude of samples in the cores and at the surface of the deposit is calculated  
118 to allow comparisons and to define relations with landsurface processes.

119 Polished thin sections of samples were observed with an optical microscope (Leica DMRXP)  
120 while scanning electron microscopy (SEM) was used for subsample investigations.

121 Manganese oxides were characterized by X-ray diffraction, using a Philips PW 1710  
122 diffractometer with a Cu-tube anode ( $k\alpha_1 = 1.78896$ ;  $k\alpha_2 = 1.79285$ ) to avoid fluorescence  
123 effects. Major chemical elements were measured out using ICP-OES.

124 When several cryptomelane generations occurred in a same sample, subsamples were  
125 extracted and identified with a capital letter (BF96-327-A and BF96-327-B) or a two-digit  
126 number (01, 02, 03, etc). The subsamples selected for  $^{39}\text{Ar}$ - $^{40}\text{Ar}$  dating were labeled with a  
127 small letter added to the sample number (e.g., BF96-632-a1 and BF96-632-f2).

128

129 **2.2. <sup>39</sup>Ar-<sup>40</sup>Ar analysis**

130

131 Samples selected for <sup>39</sup>Ar-<sup>40</sup>Ar dating were hand picked from 0.5 mm thin slabs cut from  
132 petrographic samples. They were wrapped in Al-foil to form small packets, which were  
133 stacked into a column within which packets of flux monitors were inserted every 8 to 10  
134 samples. This configuration allows determination of the vertical flux gradient with a precision  
135 as low as ± 0.2%. Samples were irradiated in the 5C position of the McMaster reactor  
136 (Hamilton, Canada) together with biotite monitor Bern4B (17.25 Ma) [Hall *et al.*, 1984], with  
137 amphibole monitor Zartman Hb3gr (1072 Ma) [Zartman, 1964; Turner, 1971; Roddick,  
138 1983], or with sanidine monitor Draz (24.99 Ma) [Wijbrans, pers. com.]. Because the sample  
139 age was unknown, 4 to 70 hours irradiations were tested [Hénocque *et al.*, 1998], 25 hours  
140 being the most suitable.

141 A VG<sup>®</sup> 3600 mass spectrometer equipped with a Daly<sup>®</sup> detector was used for analyses.  
142 Each static measurement of argon isotopes corresponds to 11 peak hopping scans.  
143 Backgrounds of the extraction and purification line were measured every first or third step  
144 and subtracted from each argon isotope of the subsequent gas fractions. Typical blank values  
145 were included in the ranges  $3.2 \times 10^{-12} < M/e40 < 4.8 \times 10^{-13}$ ,  $7.4 \times 10^{-14} < M/e39 < 4.6 \times 10^{-15}$ ,  $6.6 \times 10^{-14} < M/e38 < 3.5 \times 10^{-16}$ ,  $1.3 \times 10^{-13} < M/e37 < 1.7 \times 10^{-14}$  and  $7.6 \times 10^{-14} < M/e36 < 2.1 \times 10^{-15} \text{ cm}^3 \text{ STP}$ . All  
146 isotopic measurements were corrected for K, Ca and Cl isotopic interferences, mass  
147 discrimination and atmospheric argon contaminations. Three consecutive steps accounting for  
148 70% of the total <sup>39</sup>Ar released define a plateau age and the individual age fractions must agree  
149 within 2σ error bars of the "integrated" age of the plateau segment. Pseudo-plateau ages can  
150 be calculated, however, with less than 70% of the <sup>39</sup>Ar<sub>K</sub> released. All errors are quoted at the  
151 1σ level and do not account for <sup>40</sup>Ar\*/<sup>39</sup>Ar<sub>K</sub> ratio and monitor age uncertainty, which is  
152 included in the calculation of the plateau age error.

153

154

### 155 **3. Geographical, geomorphological and geological setting**

156

157 The Tambao Mn ore deposit is located in North Burkina Faso (14°47'N, 0°04'E) in the

158 sub-sahelian area close to a continental sedimentary basin (Figure 2). The mean annual

159 rainfall is 375 mm. The vegetation is composed of a grassy steppe alternating with forest

160 patches along river drainage axes. The Mn-ore deposit is composed of two hills

161 corresponding to lateritic landsurface relicts.

162

#### 163 **3.1. Distribution and characterization of lateritic landsurfaces**

164

165 Four major landsurfaces are observed around Tambao (Figures 1 and 2). The highest one

166 is identified on the high hill between 353 and 325 meters elevation corresponding to a relict

167 of the intermediate landsurface [*Grandin, 1976*], which bears ferricrete and/or Fe-Mn and Mn

168 pisolitic crusts [*Colin et al., 2005*]. The second landsurface observed between 325 and 300 m

169 on the highest hillslope corresponds to the high glacis, which is characterized by a quartzose

170 ferricrete incorporating reworked manganiferous and ferruginous pebbles originating from the

171 upper landsurface. The low hill also shows intermediate Fe-Mn crust relicts, the high glacis

172 being mainly represented between 325 and 300 m with a quartzose ferricrete (Figure 2). Two

173 lower landsurfaces are observed in the surrounding plain at about 300-280 m and < 280 m

174 corresponding to the middle- and low glacis, respectively. The former bears a ferricrete, while

175 the second is a sandy erosion surface.

176

#### 177 **3.2. Parent rocks and protores**

178

179 Long-term lateritic weathering of a complex parent rocks assemblage has produced a 70

180 to 80 meter thick supergene manganese ore deposit (Figures 2 and 3). The Tambao Mn-

181 deposit hosts a reserve of about 15 Mt of manganese-ore with an MnO content of 75 wt.%  
182 [*Boulanger and Sanguinetti, 1970*]. Four layers of manganese ores developed from weathered  
183 Birimian (Paleoproterozoic age) metavolcanic and metasedimentary rocks (Figure 2),  
184 composed of schist, micaschist, tuff, carbonate and quartzite [*Delfour, 1963; Grandin, 1976*].  
185 Metamorphism of the Birimian rocks is related to syn- and post-tectonic granite and  
186 granodiorite intrusions [*Picot and Trinquard, 1969*]. The metamorphic carbonates and tuffs  
187 are the main protore of the Mn deposit reflecting the mining quality of the ore [*Boulanger*  
188 *and Sanguinetti, 1970; Collins et al., 1971*], which consists of a high grade carbonate ore with  
189 hausmannite ( $Mn_3O_4$ ), a rhodochrosite-rich carbonate ore and a low grade carbonate ore  
190 containing kutnahorite ( $[Ca, Mg, Mn] CO_3$ ). About 70% of the Mn ore derives from the  
191 weathering of rhodochrosite (Figure 3) [*Picot and Trinquard, 1969*] and 30% from the  
192 weathering of spessartine rich quartzite [*Perseil and Grandin, 1978*].

193

#### 194 **4. Weathering and oxidation of protore**

195

##### 196 **4.1. Petrography**

197

198 In drill core DD2B, at altitudes ranging from 241 and 265 m (Figure 3), the parent rock is  
199 a very heterogeneous carbonate protore characterized by a ribbon pink carbonate matrix  
200 embedding thin beds (0.1-1 m thick) of manganese oxides grains, which preserve the ribbon  
201 structure. The transition between the protore and the oxidized Mn-ore is thin and partly  
202 masked by a small albitite sill in drill DD-2B (Figure 3). Between 270 and 345 m (Figure 3),  
203 the parent rock is directly replaced by the oxidized manganese ore (layer III), which also  
204 partially preserves primary structures (folds and schistosity). The top of the core (345 m) is  
205 mostly composed of detrital lateritic material. The drill core also cut across more or less  
206 weathered granite and kaolinite-rich layers between 275 and 335 m (Figure 3). The oxidation



207 of the manganese carbonate protore induced a large porosity in which botryoidal manganese  
 208 oxide aggregates developed [Hénocque et al., 1998].

209 The drill core DDH76-02 allows exploration of layers I, II and III (Figure 3). The parent  
 210 rock was not reached by the drill core but could be directly observed from outcrops.

211 Successions of manganese-rich and manganese-poor layers (10 cm thick) characterize the  
 212 quartzite formation. The manganese oxides layers deriving from the weathering of Mn-garnet  
 213 (spessartine) rich quartzite are thinner. Between 270 and 350 m, the manganese oxides  
 214 present various aspects, porous and light and/or massive and heavy with many botryoidal  
 215 concretions. In this core, manganese oxide layers alternate with weathered schist between 280  
 216 and 285 m, 300 and 310 m, and at 330 m, and with weathered granite between 315 and 325 m  
 217 and at 340 m, occurring as a quartz rich kaolinitic saprolite (Figure 3). The drill core DDH76-  
 218 09 allows investigation of layer IV, between 305 and 315 m, the lower part of the core being  
 219 composed of weathered schist between 290 and 305 m (Figure 3).

220

## 221 4.2. Mineralogy and bulk chemistry

222

223 Rhodochrosite ( $\text{MnCO}_3$ ) and/or kutnahorite ( $\text{CaMn}(\text{CO}_3)_2$ ) are the predominant primary  
 224 minerals of the carbonate protore, with small amounts of opaque minerals such as hausmanite  
 225 ( $\text{Mn}^{2+}\text{Mn}^{3+}_2\text{O}_4$ ) and hetaerolite ( $\text{ZnMn}_2\text{O}_4$ ), aligned parallel to the rock schistosity.

226 Transmitted light microscopy also reveals tephroite ( $\text{Mn}_2\text{SiO}_4$ ) and rhodonite ( $\text{MnSiO}_3$ ),  
 227 which are also oriented parallel to the rock schistosity. The weathering is characterized by *in*  
 228 *situ* transformation of rhodochrosite, hausmannite and tephroite into manganite ( $\text{MnOOH}$ ),  
 229 todorokite ( $[\text{Mn}^{2+}, \text{Mg}, \text{Ca}, \text{Ba}, \text{Na}, \text{K}]_2[\text{Mn}^{4+}, \text{Mn}^{3+}]_7\text{O}_{12} \cdot 3\text{H}_2\text{O}$ ), and pyrolusite ( $\beta\text{-MnO}_2$ ), while  
 230 spessartine ( $\text{Mn}_3\text{Al}_2[\text{SiO}_4]_3$ ) and rhodonite weathered into lithiophorite ( $[\text{Al}, \text{Li}]\text{MnO}_2[\text{OH}]_2$ ).

231 The manganese oxide ore of layer II developed according to three stages. Spessartine was  
 232 replaced by lithiophorite. The voids resulting from the dissolution of quartz, kaolinite and

233 pyrolusite are filled with cryptocrystalline cryptomelane. The manganese oxides were  
234 transformed into well-crystallized thin needles of cryptomelane (Figure 4).  
235 The weathering of the carbonate protore leads to the formation of manganite, pyrolusite and  
236 nsutite ( $\gamma\text{-MnO}_2$ ) associated with todorokite. During a first weathering stage cryptomelane  
237 occurs only in small veinlets (Figure 5a). Pyrolusite exhibits large prismatic crystals with a  
238 characteristic fracture pattern. It is transformed into cryptomelane matrices in the upper part  
239 of the deposit (Figure 5b) as indicated by the increase of  $\text{K}_2\text{O}$  (Figure 6). Multiple  
240 cryptomelane generations also occur into botryoidal aggregates (Figure 5c).

241

### 242 **4.3. Potassium sources for cryptomelane**

243

244 Because the Mn-protore do not contain much potassium (Figure 6), sources of potassium  
245 are found in the surrounding rocks of the basement and the metavolcanic and  
246 metasedimentary rocks of the Birimian Supergroup (schists, granites, granodiorites and  
247 migmatites). Large amounts of potassium can be also trapped with clay-organic molecules  
248 and also into detrital minerals like illite and micas in the upper soil horizons. The release of  
249 potassium in  $\text{Mn}^{2+}$ -rich solutions during the weathering of K-phyllosilicates into kaolinite can  
250 contribute to the formation of cryptomelane [Parc *et al.*, 1989]. The depletion of Mn and K  
251 from the upper part of the deposit was also observed during the late transformation of the  
252 massive Mn-crust into pisolitic formation, this process being contemporaneous of the major  
253 Eocene bauxitic period [Colin *et al.*, 2005]. Bauxites in the tropics formed under humid  
254 climate with a dense vegetation cover that suggests high amounts of organic acids in  
255 solutions, which can dissolve K-phyllosilicates and previously formed Mn- and K-Mn oxides,  
256 with the release of K and Mn contributing to new cryptomelane growth in oxygenated zones  
257 of the deposit.

258

## 259 **5. Geochronological investigation**

### 260 261 **5.1. $^{39}\text{Ar}$ - $^{40}\text{Ar}$ age spectra configurations**

262  
263 The stability of the K-Ar isotopic system within cryptomelane structure mainly depends  
264 on geochemical interactions with fluids. The retentivity of argon and potassium isotopes in  
265 cryptomelane has been investigated [*Lippolt et Hautmann, 1995; Vasconcelos et al., 1995;*  
266 *Vasconcelos, 1999*]. The various configurations of the age spectra obtained during  $^{39}\text{Ar}$ - $^{40}\text{Ar}$   
267 analyses have been discussed [*Vasconcelos et al., 1995; Ruffet et al., 1996; Hénocque et al.,*  
268 *1998; Hautmann et Lippolt, 2000*] that allowed definition of three types of age spectra  
269 improving the  $^{39}\text{Ar}$ - $^{40}\text{Ar}$  data interpretations.

270 Type 1 "staircase" age spectra are characterized by a rapid increase of the ages in the low  
271 temperature steps followed by a rather flat segment that allows definition of a plateau age  
272 (Figure 7a). These age spectra however suggest  $^{40}\text{Ar}^*$  losses linked to a younger weathering  
273 "episode" that could have altered the peripheral intra crystalline retention sites or induced  
274 secondary growth.

275 Type 2 "hump-shape" age spectra often show concordant "young" ages in the low and high  
276 temperature steps and "old" ages in the intermediate degassing temperatures (Figure 7b)  
277 indicating mixing of different manganese oxide generations. The low and high temperature  
278 ages are maximum estimates of the youngest generation true age, whereas the intermediate  
279 temperature ages are underestimates of the oldest generation true age.

280 Type 3 age spectra exhibit an irregular shape with a "staircase" in the low temperature steps,  
281 the ages reaching a "maximum" followed by a decrease in the second part of the spectra up to  
282 the fusion of the mineral (Figure 7c). Mixing of different mineral generations or  $^{39}\text{Ar}$  recoil  
283 during irradiation complicate the interpretation of these age spectra [*Turner and Cadogan,*  
284 *1974*], although apparently significant ages can be often obtained.

285

## 286 **5.2. $^{39}\text{Ar}$ - $^{40}\text{Ar}$ results**

287

288

289 The results were subdivided into three groups according to the altitude of the  
cryptomelane samples (Figures 8, 9, and 10).  $^{39}\text{Ar}$ - $^{40}\text{Ar}$  runs are available as an online dataset.

290

### 291 5.2.1. First group of age spectra

292

293

294 The first group of age spectra corresponds to cryptomelane samples taken between the  
groundsurface and -17 m depth, i.e., between altitudes of 342 to 325 m that are included

295 within the topographic boundaries of the intermediate landsurface (Figures 2 and 3). Fourteen

296 age spectra obtained on ten samples exhibit 4 Type 1 (staircase) and 9 Type 2 (hump) shapes

297 (Figure 8). The oldest apparent ages ( $\geq 43$  Ma) are obtained for outcrops samples Col3 and

298 BF96-190 (Figure 8a). Col3 was taken from outcropping layer III, at an altitude of 325 m, on

299 the northeastern slopes of the high hill. This sample is part of a cryptomelane vein crossing a

300 pyrolusite ore, similar to the ones developed at the transition between pyrolusite- and

301 cryptomelane domains in the drill core DD2B (Figure 6). BF96-190 corresponds to the

302 transition (at an altitude of 345 m) between the massive ore (Layer III) and the pisolitic crusts

303 [Colin *et al.*, 2005] and it is the oldest one with a pseudo plateau age at  $59.0 \pm 0.1$  Ma (45.2%

304  $^{39}\text{Ar}$  released). The age spectrum however exhibits a staircase shape with low temperature

305 apparent ages at ca 46.5 Ma indicating apparent  $^{40}\text{Ar}^*$  loss due to peripheral perturbations

306 and/or growth of a younger cryptomelane generation.

307 The four sub-samples of Col3 (b to e) are characterized by hump-shaped age spectra

308 (Figure 8a). Col3b and Col3e show the oldest pseudo plateau ages at  $48.9 \pm 0.1$  Ma and  $49.9$

309  $\pm 0.2$  Ma, respectively. Col3c shows a pseudo-plateau age at  $44.9 \pm 0.3$  Ma, and Col3d is

310 characterized by an apparent age at  $46.3 \pm 0.2$  Ma (58%  $^{39}\text{Ar}$  released). The spectra show

311 “maximum ages” as young as the magnitude of the hump is high that could indicate a mixing  
 312 of two cryptomelane generations. The ages (ca. 45-50 Ma) for Col3 are however concordant  
 313 with the ones previously obtained for two cryptomelane concretions [*Hénoque et al.*, 1998].

314 Drill core samples yield systematically younger ages than outcrop and surface samples  
 315 (Figures 8b and 8c). Samples BF96-202c3, 211, 215 and 218-a of the upper part of drill core  
 316 DDH-76-02 (342-330 m) are characterized by hump shaped age spectra with maximum  
 317 apparent ages between 34-40 Ma in the intermediate temperature steps (Figure 8b). BF96-  
 318 218a and 215 exhibit small concordant pseudo-plateau ages in the low temperature steps at  
 319  $24.6 \pm 0.8$  Ma and  $24.1 \pm 1.2$  Ma, respectively (Figure 8b). BF96-229 is a small cryptomelane  
 320 vein in the weathered granite between layers II and III in drill core DDH-76-02 (326 m) and it  
 321 displays a plateau age at  $17.8 \pm 0.1$  Ma with 64.1%  $^{39}\text{Ar}$  released (Figure 8b). The staircase  
 322 age spectrum of sample BF96-104 (327 m in Drill core DD2B) also allows definition of a  
 323 plateau age at  $17.4 \pm 0.2$  Ma with 87%  $^{39}\text{Ar}$  released (Figure 8c). Age spectra of samples  
 324 BF96-107 and BF96-108a (upper part of drill core DD-2B) display "old" and "young"  
 325 apparent ages in the low to intermediate temperature steps at  $25.6 \pm 0.4$  Ma (20% of the total  
 326  $^{39}\text{Ar}$  released) and  $17.7 \pm 0.4$  Ma (23% of the total  $^{39}\text{Ar}$  released), respectively, which are  
 327 nearly concordant with the fusion step apparent age (Figure 8c). The age-frequency diagram  
 328 (Figure 8d) reveals three major age intervals, 35-50, 23-27 and 15-18 Ma.

329

### 330 5.2.2. Second group of age spectra

331  
 332 The second group of age spectra consists of samples taken at depths ranging from -18 to -  
 333 42 m that correspond to the lower part of the cryptomelane domain at altitudes of 324 to 300  
 334 m (Figure 3), i.e., the topographic boundaries of the high glaciais landsurface (Figure 2). This  
 335 group of 19 samples (Figure 9) shows 24 age spectra with 6 Type 1 (staircase) shapes, 17  
 336 Type 2 (hump) shapes, and 1 Type 3 shape (BF96-101-b2). Samples of the high hill cores

337 (DD2B and DDH76-02) were taken within the layer III between 325 and 320 m (BF96-97,  
338 98, 101 and 102) and between 315 and 300 m (BF96-251, 256, 96, 260, 94 and 273). Samples  
339 of the low hill core were taken between 315 and 313 m (BF96-559, 561 and 563) and between  
340 309 and 300 m (BF96-571-02, 575-b and 577) (Figure 3). Sample Col1 and BF93-632-f2 are  
341 outcrop and surface sample, at altitudes of 320 m and 307 m, respectively.

342 Col1 is cryptomelane developing from metasomatism of pyrolusite (Figure 5b). Col1  
343 duplicates irradiated for 5 and 70 hours yielded very similar hump shape age spectra (Figure  
344 9a) indicating no  $^{39}\text{Ar}$  recoil during irradiation. The two age spectra show nearly concordant  
345 maximum ages in the range  $45.3 \pm 0.4 - 44.4 \pm 0.1$  Ma while one obviously shows a small  
346 pseudo-plateau age at  $27.3 \pm 0.7$  Ma derived from six concordant steps at low temperature (5  
347 to 15% of the total  $^{39}\text{Ar}$  released) that is also concordant with high temperature ages (Figure  
348 9a). BF93-632 is a hollandite concretion sampled underneath the high glaucis ferricrete at an  
349 altitude of 307 m. A sub-sample (BF96-632-a1) yields an interesting hump-shaped age  
350 spectrum with concordant low and high temperature ages at ca 16 Ma (Figure 9a). A second  
351 sub-sample (BF96-632-f2) is characterized by a staircase age spectrum with low temperature  
352 ages at ca. 16 Ma (Figure 9a), and an intermediate to high temperature pseudo-plateau age at  
353  $36.2 \pm 0.2$  Ma (46.3% of the total  $^{39}\text{Ar}$  released).

354 Samples of DD2B core are characterized by plateau ages calculated from staircase and hump-  
355 shaped age spectra around 24 Ma (Figures 9b) and at  $14.9 \pm 0.1$  Ma and  $17.1 \pm 0.1$  Ma  
356 (Figure 9c). An older plateau age was also calculated at  $28.8 \pm 0.1$  Ma (BF96-251) while four  
357 younger plateau ages are evident between  $11.5 \pm 0.2$  Ma and  $14.6 \pm 0.3$  Ma for DD76-02 core  
358 samples (Figure 9d). Sample BF96-260 with younger apparent ages (ca 21-22Ma) exhibits a  
359 clear hump shape that does not allow plateau age calculation (Figure 9d).

360 Samples of DDH76-09 core provided plateau ages at  $27.1 \pm 0.3$  Ma, and two younger at ca.  
361 24-25 Ma (Figure 9e). One sample (BF96-577) at an altitude of 304 m is characterized by a

362 unique "older" age at 36.3 Ma (Figure 9f) that is comparable with the intermediate to high  
363 temperature age of BF96-632-f2 (Figure 8a). The age frequency diagram reveals four age  
364 and/or age intervals, 12.5, 14-17, 21-25 and 27-29 Ma (Figure 9g) all being concordant with  
365 objectively calculated pseudo-plateau and plateau ages.

366

### 367 5.2.3. Third group of age spectra

368

369 The third group of age spectra consists of samples mainly taken from the pyrolusite-rich  
370 core (BF96-62, 91, 93, 299, 314, 318, 322, 327, 581, 653) between depths of -42 m to -89 m  
371 corresponding to altitudes of 300 m to 253 m, which are also the topographic ranges of the  
372 two lowest glacis (Figures 2 and 3). BF96-62 is a thin cryptomelane rim around a small  
373 pyrolusite concretion in the carbonate protore of DD2B core. Sample BF96-653 is a fragment  
374 of a cryptomelane vein crossing the exhumed schist saprolite of the low glacis. This third  
375 group includes 11 age spectra with 5 staircase and 6 hump shapes that allowed the calculation  
376 of 7 pseudo-plateau ages lower than 20 Ma (Figure 10).

377 Large error bars shown by some age spectra (BF96-62-03, BF96-91 and BF96-322)  
378 characterize the very low K<sub>2</sub>O content of these samples (e.g., 0.2 wt.% for BF96-91). Samples  
379 BF96-93 and BF96-299 of the high hill cores display plateau ages at  $11.5 \pm 0.1$  Ma and  $18.3 \pm$   
380  $0.3$  Ma, respectively (Figures 10a and 10b). The age spectrum of BF96-581 at 293 m altitude  
381 yields older apparent ages at ca. 24 Ma, which are concordant with the plateau ages obtained  
382 upper for samples BF96-561-02, 563-02 and 575-b (Figure 9e).

383 Three plateau ages were also calculated for samples BF96-653, BF96-314, BF96-318 at  
384  $5.8 \pm 0.1$  Ma,  $6.5 \pm 0.1$  and  $7.2 \pm 0.1$  Ma, respectively (Figures 10a and 10b). The hump  
385 shaped age spectrum of BF96-318 exhibits concordant apparent ages at ca. 3.5-4 Ma in the  
386 low and high temperatures. The youngest ages are displayed by three samples of DDH76-02  
387 core close to the oxidation front in the pyrolusite domain. The apparent age at ca.  $3 \pm 1.3$  Ma

388 measured for BF96-62-03 (Figure 10a) is concordant with plateau ages at  $3.4 \pm 0.1$  Ma  
389 ( $80.6\%$   $^{39}\text{Ar}$  released) and  $2.9 \pm 0.1$  Ma ( $74.7\%$   $^{39}\text{Ar}$  released) yielded by samples BF96-327-  
390 a1 and -327-a2, respectively (Figure 10b). Ages at 5.5-7.5 Ma and ca. 3 Ma are well depicted  
391 by the age frequency diagram, which also reveals ages at 11.5, 18 and 22.5 Ma (Figure 10c).  
392

## 393 **6. $^{39}\text{Ar}$ - $^{40}\text{Ar}$ ages interpretation**

394  
395 The oldest ages (ca. 59 Ma to ca. 45 Ma) obtained for cryptomelane of outcrop and  
396 surface samples (Figure 8a) are coherent with the ages of massive Mn-crust and pisolites  
397 [*Colin et al.*, 2005], and also the ages of botryoidal concretions [*Hénoque et al.*, 1998].  
398 These ages indicate a sustained humid and warm paleoclimate for at least 14 Ma that could  
399 represent the duration of the Eocene bauxite formation period. The age ca. 49 Ma obtained for  
400 a cryptomelane at -25 m depth (Col 3) allows estimation of  $2.5 \text{ m. Ma}^{-1}$  for the oxidation front  
401 sinking rate between 59 and 49 Ma. However, the staircase and hump shapes of age spectra of  
402 drill core samples in the highest part of layers I, II and III suggests a reactivation of  
403 geochemical weathering process, and thus a rejuvenation of older minerals (Figure 8).  
404 Concentric banded overgrowth structures (e.g., botryoidal) effectively result from repeated  
405 geochemical mobilizations of Mn and K that led to newly formed cryptomelane generations  
406 (Figure 5c). Their crystal size is so small that handpicking sampling inevitably implied  
407 mixings of “old” and “young” generations characterized by hump-shaped age spectra, with  
408 maximum apparent ages in the range 40-33 Ma and lower than the plateau and pseudo-plateau  
409 ages of outcrop samples (Figure 8a).

410 The age spectra of the first group document two subsequent weathering episodes (Figure  
411 8d). An episode at ca 27-23 Ma is obviously defined in the upper part of the cryptomelane  
412 domain as shown by the diagram of plateau and pseudoplateau ages *vs.* altitude where the  
413 elevation ranges of each lateritic landsurface are also represented (Figure 11a). This episode



414 was also characterized in the pisolitic crust [*Colin et al.*, 2005], where it superimposed to the  
415 lateritic episode at ca. 46 Ma. The lower part of the cryptomelane domain also yields  
416 reproducible pseudo-plateau and plateau ages in the range 29-24 Ma (Figure 9) that could  
417 document the downward propagation of the oxidation front at an average rate of 2 m. Ma<sup>-1</sup>.  
418 Another weathering episode is depicted by low temperature ages around 18-17 Ma (Figures  
419 8b, 8c and 8d). Plateau ages at 18-17 Ma were also obtained in the lower part of the  
420 cryptomelane domain and for vein cryptomelane of the upper pyrolusite domain (Figures 9c  
421 and 10b) that further supports the likelihood of this weathering episode.

422 The youngest ages, ca. 18 to ca. 3 Ma, document active weathering and oxidation  
423 processes during the Neogene. Cryptomelane often crystallized in small veins and concretions  
424 in the pyrolusite rich lower parts of the deposit indicating episodic deep circulations of  
425 weathering solutions. The cryptomelane crystals are characterized by plateau ages ranging  
426 between 17.8 Ma and 2.9 Ma (Figure 10), and these ages are as young as samples collected  
427 close to the oxidation front (Figure 11a). Figure 11a also includes <sup>39</sup>Ar-<sup>40</sup>Ar ages obtained by  
428 previous studies [*Henocque et al.*, 1998; *Colin et al.*, 2005]. Figure 11b shows less apparent  
429 age scattering and increasing purity of analyzed parageneses with depth.

430 Although the increasing diversity of <sup>39</sup>Ar-<sup>40</sup>Ar ages from the bottom to the top of the Mn-  
431 deposit (Figure 11b) suggests a continuous chemical weathering for 59 Ma, five main  
432 weathering periods can be differentiated. The first from ca. 59 Ma to ca. 45 Ma characterizes  
433 a long weathering period, during which bauxites formed all over the tropical belt [*Bardossy  
434 and Aleva*, 1990]. The second occurred in the range 29-24 Ma with an occurrence at 21 Ma  
435 (Figure 11a), and it was well depicted in the ore deposit (Figure 9). The intermediate  
436 landsurface was also deeply weathered during this major period. The three last periods are  
437 characterized by short weathering episodes, 18-11.5 Ma, 7.2 -5.8 Ma and 3.4-2.9 Ma (Figure

438 11a), during which the three glacis were probably weathered along with recurrences between  
439 18-11.5 Ma in the pre-existing intermediate landsurface profile (Figure 11a).

440

## 441 **7. Lateritic weathering, palaeoclimates, long-term morphogenesis and denudation**

442

443 Petrographical and geochemical patterns of the different lateritic landsurfaces and the  
444 height difference between the landsurfaces reflect differences in duration and intensity of  
445 weathering and erosion processes linked to contrasted paleoclimates between the Palaeogene  
446 and Neogene [*Tardy and Roquin, 1998*]. The comparison of the global  $\delta^{18}\text{O}$  and eustatic  
447 curves [*Miller et al., 2005*] with  $^{39}\text{Ar}$ - $^{40}\text{Ar}$  ages distribution (Figures 12a, 12b and 12c) and  
448 with the intracontinental sedimentary sequences (Figure 13a) contributes to a better  
449 understanding of the influence of Cenozoic paleoclimatic changes on West African  
450 landscapes. The age frequency histogram in Figure 12c incorporates all the results including  
451 those obtained from the previous studies [*Henocque et al., 1998; Colin et al., 2005*]. The  
452 series of  $^{39}\text{Ar}$ - $^{40}\text{Ar}$  ages and time intervals between these ages may document, as a surrogate  
453 for long-term paleoclimatic proxies, the major chemical weathering (warm/humid climate)  
454 and mechanical erosion (cold/dry climate) periods (Figures 12 and 13b). The altitude of dated  
455 samples and the elevation (maximum) of each planation landsurface allow estimation of  
456 average mechanical erosion rate for different time spans corresponding to the successive  
457 lateritic planation cycles.

458

459 From Paleocene (ca. 60 Ma) to middle Lutetian (ca. 45 Ma),  $\delta^{18}\text{O}$  is low and the eustatic  
460 level is high [*Zachos et al., 2001; Miller et al., 2005*] (Figure 12a and 12b). The identification  
461 of marine sediment incursions between the “Continental Intercalaire” and the basal  
462 unconformity in the Iullemeden basin, 150 km North North-East and East of Tambao  
463 (Figure 13a) indicates a maximal extension of the Saharan sound between 55 and 60 Ma in  
western Niger [*Petters, 1977*]. The marine sediments are mainly composed of carbonates,

464 marls, and clays dominated by sepiolite, palygorskite and attapulgite [Millot, 1970; Chamley  
465 *et al.*, 1988; Ly and Anglada, 1991] that characterize biogeochemical sedimentation. This was  
466 also linked to the genesis of thick bauxitic weathering mantles inland including a differential  
467 sequestration of Fe and Mn according to their respective chemical mobility.

468 Bauxites have been described on Precambrian basement and also upon the unconformity  
469 (Figure 13a) between the “Continental Intercalaire” deposits and the siderolithic “Continental  
470 Terminal” (CT) in the Iullemeden basin [Faure, 1966; Gavaud, 1977; Lang *et al.*, 1990].  
471 The basal sequence of CT (Upper Lutetian) is characterized by oolites, which are also  
472 interstratified within the upper siderolithic sediments [Boudouresque *et al.*, 1982]. This  
473 suggests that dissolved iron input originated from inland lateritic formations, whereas the  
474 siderolithic detrital sediments corresponds to the mechanical erosion of lateritic weathering  
475 mantles according to alternating humid and dry palaeoclimates, respectively. A ferricrete  
476 specific of the intermediate surface has also been described upon the CT sediments (Figure  
477 13a) of Mali and Niger [Gavaud, 1977; Lang *et al.*, 1990]. Relicts of a similar ferricrete are  
478 also present on the high hill where  $^{39}\text{Ar}$ - $^{40}\text{Ar}$  ages of 59-45 Ma and also 29-24 Ma were  
479 measured. The field observations and  $^{39}\text{Ar}$ - $^{40}\text{Ar}$  data imply that the bauxitic and intermediate  
480 ferruginous paleolandscapes intersected near the Tambao Mn-deposit (Figure 13a), thus  
481 questioning the supposed Pliocene age of the ferricrete upon the CT sediments [Michel, 1973;  
482 Grandin, 1976; Gavaud, 1977].

483 Biogeochemical sedimentation ceased in mid-Eocene (Lutetian) as indicated by the  
484 marine sedimentary gap at the bottom of Iullemeden [Faure, 1966; Boudouresque *et al.*,  
485 1982] and Senegalese basins [Ly, 1985]. This gap might be correlated to the sea level drop  
486 between ca. 34 Ma and ca. 29 Ma [Miller *et al.*, 2005] (Figure 12b) that resulted from  
487 Oligocene global cooling concomitant with the development of East Antarctic Ice Sheet  
488 [Salamy and Zachos, 1999; Zachos *et al.*, 2001]. These changes have induced drier climatic

489 conditions on continents [Lawver *et al.*, 1992], with an apogee at ca 33.5 Ma [Kennett and  
490 Shackleton, 1976; Zachos *et al.*, 1994, 1996; Salamy and Zachos, 1999; Miller *et al.*, 2005]  
491 and a persistence until the Middle Oligocene-Early Miocene [Flower and Kennett, 1994] as  
492 indicated by  $\delta^{18}\text{O}$  increase [Miller *et al.*, 2005] (Figure 12a). No significant  $^{39}\text{Ar}$ - $^{40}\text{Ar}$  ages  
493 were obtained in the range 45-29 Ma (Figure 12c). Following the eustatic change, the  
494 progressive sea retreat towards north and south [Faure, 1966] led to the incision and erosion  
495 of previous lateritic landforms. An average mechanical erosion rate of  $3 \text{ m. Ma}^{-1}$  can be  
496 calculated for the period 45-29 Ma assuming an elevation of 400 m for the warped bauxitic  
497 landsurface, and the intermediate surface at 350 m (Figure 13a). At that time, continental  
498 sedimentation (siderolithic CT) could include lateritic materials eroded from early bauxitic  
499 and clay-ferruginous weathering mantles. The bauxite erosion allowed the exhumation of  
500 ferruginous materials, i.e., the formation of the ferricrete-bearing intermediate landsurface.

501 The next major episode of chemical weathering in Tambao occurred around 29-24 Ma  
502 (Figure 12c) corresponding with late Oligocene global warming [Zachos *et al.*, 2001] and to a  
503 relative stability of the global sea level [Miller *et al.*, 2005]. This age interval was particularly  
504 well represented in the Mn-ore deposit (Figure 9b) and could date the weathering of the  
505 recently exhumed intermediate lateritic profiles (Figures 11a and 13b) and also the formation  
506 of the older ferricrete observed upon the Iullemeden CT sediments (Figure 13a).

507 Although Milankowitch glacial-interglacial cycles are well documented in the Oligocene  
508 [Retallack *et al.*, 2004], the global Earth climate was frankly driven by a glacial-interglacial  
509 dynamic from the boundary Oligocene/Miocene [Zachos *et al.*, 2001]. The three ferruginous  
510 glacis could be formed between 24 and 3 Ma as results of the alternation of mechanical  
511 erosion and chemical weathering episodes (Figures 12 and 13b) according to low frequency  
512 climatic oscillations but higher seasonality. Except an age at ca 21 Ma, the interval 24-18 Ma  
513 could have been propitious to the mechanical erosion of the intermediate landsurface at an

514 average rate of 4 m. Ma<sup>-1</sup>, at least partially, and to the final denudation of bauxitic remnants.  
515 This major mechanical erosion episode led to the setting of the high glacis, which was  
516 weathered at 18-17 Ma, 15-14.5 Ma and 12.7-11.5 Ma (Figures 11a, 12c and 13b) as  
517 suggested by the increase of  $\delta^{18}\text{O}$  and the relatively high sea level [*Berger and Wefer, 1996;*  
518 *Miller et al., 2005*] (Figures 12a and 12b). Coarser lateritic materials including bauxite and  
519 ferricrete debris were also reworked into the newly formed high glacis landsurface that is  
520 characteristic of glacis-forming processes under drier climatic conditions [*Vogt, 1959; Michel,*  
521 *1973, 1978; Grandin, 1976; Boulangé and Millot, 1988; Thomas, 1994*]. Notice also that the  
522 weathering of intermediate surface remnants could have been reactivated between 18 and 11.5  
523 Ma (Figure 11a) confirming observations in other West African areas [*Beauvais et al., 1999,*  
524 *2004*]. The interval 11.5-7.2 Ma would correspond to the mechanical erosion of the high  
525 glacis at an average rate of 6 m. Ma<sup>-1</sup> leading to the middle glacis emplacement before it's  
526 weathering at 7.2-5.8 Ma. A short erosive episode from ca. 5.8 to 3.4 Ma at an average rate of  
527 8 m. Ma<sup>-1</sup>, which is comparable with the previously estimated erosion rate using cosmogenic  
528 nuclides [*Brown et al., 1994*], allowed emplacement of the low glacis, before this latter was  
529 weathered at ca 3.4-2.9 Ma (Figure 13b).

530

## 531 **8. Conclusion**

532

533 <sup>39</sup>Ar-<sup>40</sup>Ar ages were obtained on different cryptomelane generations sampled on outcrops  
534 and drill cores in the Mn-ore deposit of Tambao (North Burkina Faso), which mainly  
535 developed from the oxidation of carbonate and silicate protores. The <sup>39</sup>Ar-<sup>40</sup>Ar ages were  
536 compared with the variations of the global  $\delta^{18}\text{O}$  and eustatic curves that documented  
537 successive Cenozoic chemical weathering and mechanical erosion periods driven by the  
538 alternation of warm/humid climates and cold/dry climates, respectively. The interval 59-45  
539 Ma corresponds to the Eocene bauxitic period, implying that cryptomelane formed during

540 warm and humid periods in well-oxygenated lateritic weathering profiles. However, bauxite  
541 ferruginization and thus the starting of ferricrete individualization in the profiles characterized  
542 the end of this period, ca. 50 to ca. 45 Ma. The lack of significant measured ages from ca. 45  
543 Ma to ca. 29 Ma corresponds to a period dominated by incision and erosion processes under  
544 drier climatic conditions, during which continental sediments started to accumulate in West  
545 African intracratonic basins. The intermediate landsurface was probably formed at the end of  
546 this period (ca. 34 to ca. 29 Ma). Then the newly exposed lateritic landsurface was further  
547 weathered between 29 and 24 Ma. This age interval could also date the ferricrete upon  
548 Iullemeden CT sediments. The high glacia could have been shaped in the interval of 24-18  
549 Ma, weathered around 18-17, 15-14 and 12.7-11.5 Ma, and eroded between 11.5 and 7.2 Ma,  
550 an interval propitious to the settlement of the middle glacia before this one was weathered at  
551 7.2-5.8. The lowest glacia was shaped in the interval 5.8-3.4 Ma before the last short chemical  
552 weathering episode at 3.4-2.9 Ma. Our results allow average estimations of the oxidation front  
553 sinking rate of 2.5 m. Ma<sup>-1</sup> for the period 59-45 Ma against 1.5 m. Ma<sup>-1</sup> for the period 59-3  
554 Ma. The average erosion rates of the successive lateritic landsurfaces would be 3 to 8 m. Ma<sup>-1</sup>  
555 for the period 59-3 Ma. However, persistence of lateritic landsurface relicts in the landscape,  
556 and old cryptomelane (59-45 Ma) in the upper part of the ore deposit, indicates low Cenozoic  
557 denudation rates, of the order of the height differences between the lateritic landsurfaces.

558  
559 **Acknowledgments** – This is a contribution of CEREGE (UMR IRD 161), with financial  
560 support from DBT-PROSE and IRD scientific programs. We specially thank Dr. Georges  
561 Grandin and Dr. Dominique Chardon for fruitful discussions. Dominique Chardon is also  
562 gratefully acknowledged for artwork of the figure 13a.

563

563 **References**

- 564 Aleva, G.J.J. (1984), Lateritisation, bauxitisation and cyclic landscape development in the  
565 Guiana shield, in *Bauxite*, proceedings 1984 bauxite symposium, edited by L. Jacob Jr., pp.  
566 111-151, AIME, New York.
- 567 Bardossy, G., and G.J.J. Aleva (1990), *Lateritic bauxites*, Elsevier, Amsterdam.
- 568 Beauvais, A., A. Melfi, D. Nahon, and J.J. Trescases (1987), Pétrologie du gisement  
569 latéritique manganésifère d'Azul (Brésil), *Miner. Deposita*, 22, 124-134.
- 570 Beauvais A., M. Ritz, J-C. Parisot, M. Dukhan, and C. Bantsimba (1999), Analysis of poorly  
571 stratified lateritic terrains overlying a granitic bedrock in West Africa, using 2D electrical  
572 resistivity tomography, *Earth Planet. Sci. Letters*, 173, 413-424.
- 573 Beauvais A., M. Ritz, J-C. Parisot, C. Bantsimba, and M. Dukhan (2004), Combined ERT and  
574 GPR methods for investigating two stepped lateritic weathering systems, *Geoderma*, 119,  
575 121-132.
- 576 Berger, W.H., and G. Wefer (1996), Expeditions into the past: Paleoceanographic studies in  
577 the south Atlantic, in *The south Atlantic: present and past circulation*, edited by G. Wefer  
578 et al., Springer editions.
- 579 Boudouresque, L., D. Dubois, J. Lang, and J. Trichet (1982), Contribution to the stratigraphy  
580 and paleogeography of the western edge of the Iullemmeden basin during the upper  
581 Cretaceous and Cenozoic (Niger and Mali – West Africa), *Bull. Soc. Géol. France*, 24,  
582 685-695.
- 583 Boulangé, B., and G. Millot (1988), La distribution des bauxites sur le craton Ouest Africain,  
584 *Sci. Géol. Bulletin*, 41, 113-123.
- 585 Boulanger, J.J., and H. Sanguinetti (1970), Evaluation générale du gisement de manganèse  
586 de Tambao. Haute Volta, Enquêtes sur le développement minier dans le nord-est et  
587 facteurs associés de transport, *Rapport n°3*, 48 pp., PNUD, Ouagadougou, Burkina Faso.

- 589 Brown, T.E., D.L. Bournès, F. Colin, Z. Sanfo, G.M. Raisbeck, and F. Yiou (1994), the  
590 development of iron crust lateritic systems in Burkina Faso, West Africa examined with in-  
591 situ-produced cosmogenic nuclides, *Earth Planet. Sci. Letters*, 124, 19-33.
- 592 Burns, R.G., and V.M. Burns (1979), Manganese oxides, in *Marine minerals*, edited by P.H.  
593 Ribbe, pp. 1-46, Mineral. Soc. Am., Washington DC.
- 594 Chamley, H., P. Debrabant, and R. Flicoteaux (1988), Comparative evolution of the Senegal  
595 and eastern central Atlantic basins, from mineralogical and geochemical investigations,  
596 *Sedimentology*, 35, 85-103.
- 597 Chevillotte, V., D. Chardon, A. Beauvais, P. Maurizot, and F. Colin (2006), Long-term  
598 tropical morphogenesis of New Caledonia (Southwest Pacific): importance of positive  
599 epirogeny and climate change, *Geomorphology*, 81, 361-375.
- 600 Chukhrov, F.V., L.L. Shanin, and L.P. Yermilov (1966), Feasibility of absolute-age  
601 determination for potassium-carrying manganese minerals, *Int. Geol. Rev.*, 8, 278-280.
- 602 Colin, F., A. Beauvais, G. Ruffet, and O. Hénocque (2005), First  $^{40}\text{Ar}/^{39}\text{Ar}$  geochronology of  
603 lateritic manganiferous pisolites: Implications for the palaeogene history of a West African  
604 landscape, *Earth Planet. Sci. Letters*, 238, 172-188.
- 605 Collins, D.N., A.R. Tron, J.C. Wilson, and P. Parsonage (1971), The treatment of Tambao  
606 Manganese Ore deposit for United Nations, *Unpublished report*, 24pp., Warren Spring  
607 Laboratory, Department of trade and industry, CR504.
- 608 Dasgupta, S., S. Roy, and M. Fukuoka (1992), Depositional models for manganese oxides  
609 and carbonates deposits of the Precambrian Sausar group, India, *Econ. Geol.*, 87(5), 1412-  
610 1418.
- 611 Delfour, J. (1963), Géologie du gîte de manganese de Tambao (haute-Volta), *Unpublished*  
612 *BRGM report 5612*, 20 pp., BRGM, Orléans, France.



- 613 Faure, H. (1966), Reconnaissance géologique des formations sédimentaires post-  
614 paléozoïques du Niger oriental, Doct sci. Thesis, Univ. Paris, Mém. B.R.G.M., 47,  
615 Orléans, France.
- 616 Flower, B.P., and J.P. Kennett (1994), The middle Miocene climatic transition: East  
617 antarctic ice sheet development, deep ocean circulation and global carbon cycling, *Science*,  
618 *108*(3/4), 537-555.
- 619 Gavaud, M. (1977), Les grands traits de la pédogenèse au Niger méridional, Travaux et  
620 Documents ORSTOM, 76, 104 pp., Paris, France.
- 621 Grandin, G. (1976), Aplanissements cuirassés et enrichissement des gisements de  
622 manganèse dans quelques régions d'Afrique de l'Ouest, Doct sci. thesis, Univ. Strasbourg,  
623 Mém. ORSTOM, 82, Paris, France.
- 624 Gunnell, Y. (2003), radiometric ages of laterites and constraints on long-term denudation  
625 rates in West Africa, *Geology*, *31*(2), 131-134.
- 626 Hall, C.M., R.C. Walter, J.A. Westgate, and D. York (1984), Geochronology, stratigraphy  
627 and geochemistry of Cindery tuff in Pliocene hominid-bearing sediments of the middle  
628 Awash, Ethiopia, *Nature*, *308*, 26-31.
- 629 Hautmann, S., and H.J. Lippolt (2000),  $^{40}\text{Ar}/^{39}\text{Ar}$  dating of central European K-Mn oxides a  
630 chronological framework of supergene alteration processes during the Neogene, *Chem.*  
631 *Geol.*, *170*(1-4), 37-80.
- 632 Hénocque, O., G. Ruffet, F. Colin, and G. Féraud (1998),  $^{40}\text{Ar}/^{39}\text{Ar}$  dating of West African  
633 lateritic cryptomelanes, *Geochim. Cosmochim. Acta*, *62*(16), 2739-2756.
- 634 Kennett, J.P., and N.J. Shackleton (1976), Oxygen isotopic evidence for the development of  
635 the psychrosphere 38 Ma ago, *Science*, *260*, 513-515.
- 636 King, L.C. (1967), *The morphology of the Earth. A study and synthesis of world scenery*,  
637 2nd ed., Olivier & Boyd, Edinburgh, Scotland.

- 638 Lang, J., C. Kogbe, S. Alidou, K. A. Alzouma, G. Bellion, D. Dubois, A. Durand, R.  
639 Guiraud, A. Houessou, I. de Klasz, E. Romann, M. Salard-Cheboldaeff, and J. Trichet  
640 (1990), The continental terminal of West Africa, *J. Afr. Earth Sci.*, 10(1-2), 79-99.
- 641 Lawver, L.A., L.M. Gahagan, and M.F. Coffin (1992), The development of paleoseaways  
642 around Antarctica, in *The Antarctic Paleoenvironment: A perspective on global change*,  
643 edited by L.P. Kennett and D.A. Warnke, pp. 7-30, Antarctic Research Series, 56.
- 644 Lippolt, H.J., and S. Hautmann (1995),  $^{40}\text{Ar}/^{39}\text{Ar}$  ages of Precambrian manganese ore  
645 minerals from Sweden, India and Morocco, *Miner. Deposita*, 30, 246-256.
- 646 Ly, A. (1985), Le Tertiaire de Casamance (Sénégal) : Biostratigraphie (Foraminifères) et  
647 sédimentologie d'après les données de subsurface, Doct. sci. Thesis, 215 pp., Univ. Aix-  
648 Marseille III, Marseille, France.
- 649 Ly, A., and R. Anglada (1991), Le Bassin Sénégal-Mauritanien dans l'évolution des marges  
650 périatlantiques au Tertiaire, *Cahiers de Micropaléontologie*, 6, 2, 23- 40.
- 651 Michel, P. (1973), Les Bassins des fleuves Sénégal et Gambie : étude géomorphologique,  
652 Doct sci. Thesis, Univ. Strasbourg, Mém. ORSTOM, 63, Paris, France.
- 653 Michel, P. (1978), Cuirasses bauxitiques et ferrugineuses d'Afrique Occidentale Aperçu  
654 chronologique, *Trav. Doc. Géogr. Trop.*, 33, pp. 11-32, CEGET CNRS, Bordeaux, France.
- 655 Miller, K. G., M. A. Kominz, J. V. Browning, J. D. Wright, G. S. Mountain, M. E. Katz, P.  
656 J. Sugaman, B. S. Cramer, N. Christie-Blick, and S. F. Pekar (2005), The phanerozoic  
657 record of global sea-level change, *Science*, 310, 1293-1298.
- 658 Millot, G. (1970), *Geology of clays*, Chapman and Hall, London.
- 659 Millot, G. (1983), Planation of continents by intertropical weathering and pedogenetic  
660 processes, in *lateritisation processes*, pp. 53-63, edited by A. J. Melfi and A. Carvalho,  
661 Proceedings of the II<sup>nd</sup> international Seminar on Lateritisation Processes, Sao Paulo, Brazil.

- 662 Nahon, D. (1991), *Introduction to the petrology of soils and chemical weathering*, John  
663 Wiley and sons, New York.
- 664 Nahon, D., A. Beauvais, P. Nziengui-Mapangou, and J. Ducloux (1984), Chemical  
665 weathering of Mn-garnets under lateritic conditions in northwest Ivory Coast (West  
666 Africa), *Chem. Geol.*, 45, 53-71.
- 667 Nahon, D., B. Boulangé, and F. Colin (1992), Metallogeny of weathering: an introduction, in  
668 *Weathering, soils & paleosols*, pp. 445-467, edited by I.P. Martini and W. Chesworth,  
669 Developments in Earth Surface Processes 2, Elsevier, Amsterdam.
- 670 Oswald, J. (1992), Genesis and paragenesis of the tetravalent manganese oxides of the  
671 Australian continent, *Econ. Geol.*, 87(5), 1237-1253.
- 672 Parc S., D. Nahon, Y. Tardy, and P. Vieillard (1989), Estimated solubility products and field  
673 of stability for cryptomelane, nsutite, birnessite and lithiophorite based on natural lateritic  
674 weathering sequences, *Amer. Miner.*, 74, 466-475.
- 675 Partridge, T.C., and R.R. Maud (1987), Geomorphic evolution of Southern Africa since the  
676 Mesozoic, *S. Afr. J. Geol.*, 90, 179-208.
- 677 Pedro, G. (1968), Distribution des principaux types d'altération chimique à la surface du  
678 globe, *Rev. Géogr. Phys. Géol. Dyn.*, 10(5), 457-470.
- 679 Perseil E.A., and G. Grandin (1978), Evolution minéralogique du manganèse dans trois  
680 gisements d'Afrique de l'Ouest : Mokta, Tambao, Nsuta. *Miner. Deposita*, 13, 295-311.
- 681 Petters S.W. (1977), Ancient Seaway across the Sahara, *Nigerian Field*, 42, 23-31.
- 682 Picot P., and R. Trinquard (1969), La manganosite (MnO) du gîte de manganèse de Tambao  
683 (Haute-Volta), *Bull. Soc. fr. Minér. Cristallogr.*, 92, 500-502.
- 684 Pracejus B., and B.R. Bolton (1992), Geochemistry of supergene manganese oxide deposits,  
685 Groote Eylandt, Australia, *Econ. Geol.*, 87(5), 1310-1335.

- 686 Retallack G.J., J.G Wynn, and T.J. Fremd (2004), Glacial-interglacial-scale paleoclimatic  
687 change without large ice sheets in the Oligocene of central Oregon, *Geology*, 32(4), 297-  
688 300.
- 689 Roddick J. C. (1983), High precision intercalibration of  $^{40}\text{Ar}/^{39}\text{Ar}$  standards. *Geochim.*  
690 *Cosmochim. Acta*, 47, 887-898.
- 691 Roy S. (1981), *Manganese deposits*, Academic press, London.
- 692 Roy S. (1988), Manganese metallogenesis : a review, *Ore Geol. Rev.*, 4(1-2), 155-170.
- 693 Ruffet G., C. Innocent, A. Michard, G. Féraud, A. Beauvais, D. Nahon, and B. Hamelin  
694 (1996), A geochronological  $^{40}\text{Ar}/^{39}\text{Ar}$  and  $^{87}\text{Rb}/^{87}\text{Sr}$  study of K-Mn oxides from the  
695 weathering sequence of Azul (Brazil), *Geochim. Cosmochim. Acta*, 60, 2219-2232.
- 696 Salamy K.A., and J.C. Zachos (1999), Latest Eocene-Early Oligocene climate change and  
697 Southern Ocean fertility : inferences from sediment accumulation and stable isotope data,  
698 *Pal. Pal. Pal.*, 145, 61-77.
- 699 Segev A., L. Halicz, B. Lang, and G. Steinitz (1991), K-Ar dating of manganese minerals  
700 from the Eisenbach region, Black Forest, Southwest Germany, *Schweiz. Mineral. Petrogr.*  
701 *Mitt.*, 71, 101-114.
- 702 Tardy Y., and C. Roquin (1998), *Dérive des continents, paléoclimats et altérations*  
703 *tropicales*, BRGM, Orléans, France.
- 704 Thomas, M.F. (1994), *Geomorphology in the tropics. A study of weathering and denudation*  
705 *in low latitudes*, Wiley, New York.
- 706 Turner G. (1971),  $^{40}\text{Ar}$ - $^{39}\text{Ar}$  ages from the lunar maria, *Earth Planet. Sci. Lett.*, 11, 169-191.
- 707 Turner G., and P.H. Cadogan (1974). Possible effects of  $^{39}\text{Ar}$  recoil in  $^{40}\text{Ar}$ - $^{39}\text{Ar}$  dating, paper  
708 presented at 5th lunar Conference, 2, 1601-1615.
- 709 Turner S., and P.R. Buseck (1979), Manganese Oxide Tunnel Structures and their  
710 Intergrowths, *Science*, 203, 456-458.

- 711 Varentsov I.M., and D.I. Golovin (1987), Groote Eylandt Manganese deposit, North  
712 Australia : K-Ar age of cryptomelane ores and aspects of genesis, *Reports Acad. Sci.*  
713 USSR, 294(1), 203-207.
- 714 Varentsov I.M. (1996), *Manganese ores of supergene zone : geochemistry of formation*,  
715 Kluwer Academic Publisher, Dordrecht, The Netherlands.
- 716 Vasconcelos P.M. (1999), K-Ar and  $^{40}\text{Ar}/^{39}\text{Ar}$  geochronology of weathering processes, *Annu.*  
717 *Rev. Earth Planet. Sci.*, 27, 183-229.
- 718 Vasconcelos P.M., T.A. Becker, P.R. Renne, and G.H. Brimhall (1992), Age and duration of  
719 weathering by  $^{40}\text{K}$ - $^{40}\text{Ar}$  and  $^{40}\text{Ar}/^{39}\text{Ar}$  analysis of Potassium-Manganese Oxides, *Science*,  
720 58, 451-455.
- 721 Vasconcelos P.M., P.R. Renne, T.A. Becker, and H.R. Wenk (1995), Mechanisms and  
722 kinetics of atmospheric, radiogenic, and nucleogenic argon release from cryptomelane  
723 during  $^{40}\text{Ar}/^{39}\text{Ar}$  analysis, *Geochim. Cosmochim. Acta*, 59(10), 2057-2070.
- 724 Vasconcelos P.M., P.R. Renne, G.H. Brimhall, and T.A. Becker (1994), Direct dating of  
725 weathering phenomena by  $^{40}\text{Ar}/^{39}\text{Ar}$  and K-Ar analysis of supergene K-Mn oxides,  
726 *Geochim. Cosmochim. Acta*, 58, 1635-1665.
- 727 Vogt, J. (1959), Aspects de l'évolution géomorphologique récente de l'Ouest africain, *Ann.*  
728 *Géogr. Fr.*, 68(367), 193-206.
- 729 Yashvili L.P., and R.K. Gukasyan (1974), Use of cryptomelane for potassium-argon dating  
730 of manganese ore of the Sevkar-Sargyukh deposit, Armenia, *Doklady Earth Sci. Sect.*, 212,  
731 49-51.
- 732 Zachos J.C., M. Pagani, L. Sloan, E. Thomas, and K. Billups (2001), Trends, rhythms, and  
733 aberrations in global climate 65 Ma to present, *Science*, 292, 686-693.

734 Zachos J.C., T.M. Quinn, and K.A. Salamy (1996), High-resolution (104 years) deep-sea  
735 foraminiferal stable isotope records of the Eocene-Oligocene climate transition,  
736 *Paleoceanography*, 11(3), 251-266.

737 Zachos J.C., L.D. Stott, and K.C. Lohmann (1994), Evolution of early Cenozoïque marine  
738 temperatures, *Paleoceanography*, 9(2), 353-387.

739 Zartman R. E. (1964), A geochronological study of the Love Grove Pluton from the Llano  
740 uplift, Texas, *Journal of Petrology*, 5, 359-408.

741

741 **Figures caption**

742

743 Figure 1. Synthetic geomorphological sequence of lateritic paleolandsurfaces in West Africa

744 (The rectangle defines the Tambao sequence in North Burkina Faso).

745

746 Figure 2. Location and geomorphologic patterns of the Mn-ore deposit of Tambao in North

747 Burkina Faso, with the locations of the drill cores, and a section (A-B) across the main

748 geological formations (blue circle in the inset = intracratonic sedimentary basin).

749

750 Figure 3. Logs of the drill cores with the locations of samples dated by the  $^{39}\text{Ar}$ - $^{40}\text{Ar}$  method.

751

752 Figure 4. (a) SEM photomicrograph of cryptomelane needles with (b) its chemical analysis.

753

754 Figure 5. Photomicrographs of (a) cryptomelane (C) vein, (b) cryptomelane (C) developing

755 from the metasomatism of pyrolusite (P), and (c) botryoidal cryptomelane.

756

757 Figure 6. Geochemical evolution along DD2B drill core.

758

759 Figure 7.  $^{39}\text{Ar}$ - $^{40}\text{Ar}$  age spectra configuration, (a) Type 1 (stair case), (b) Type 2 (hump) shape

760 and (c) Type 3. (ca. = concordant apparent ages)

761

762 Figure 8.  $^{39}\text{Ar}$ - $^{40}\text{Ar}$  age spectra of cyptomelane extracted from the upper part of the deposit

763 (342-325 m altitudes), (a) outcrop and intermediate surface samples, (b) DDH76-02 drill

764 core, (c) DD2B drill core, and (d) frequency diagram of apparent ages. (See figure 3 for

765 sample locations).

766

767 Figure 9.  $^{39}\text{Ar}$ - $^{40}\text{Ar}$  age spectra of cyptomelane extracted from the upper and middle parts of

768 the deposit (325-300 m altitudes), (a) outcrop samples, (b) and (c) DD2B drill core, (d)

769 DDH76-02 drill core, (e) and (f) DDH76-09 drill core, and (g) frequency diagram of

770 apparent ages. (See figure 3 for sample locations).

771 Figure 10.  $^{39}\text{Ar}$ - $^{40}\text{Ar}$  age spectra of cyptomelane extracted from the lower part of the deposit  
 772 (300-253 altitudes), (a) samples from DD2B, DDH76-09 drill cores and low glacia (b)  
 773 DDH76-02 drill core, and (c) frequency diagram of apparent ages. (See figure 3 for sample  
 774 locations).

775  
 776 Figure 11. (a) Distribution of pseudo-plateau and plateau ages as a function of altitude in the  
 777 Mn-deposit with the superimposition of the elevation ranges of each landsurface (b) 3D  
 778 frequency diagram of all apparent ages versus altitude. (Curved black arrow = decreasing  
 779 chemical weathering and increasing erosion rate).

780  
 781 Figure 12. Comparison between the global curves of (a)  $\delta^{18}\text{O}$ -paleotemperatures and (b)  
 782 eustatic levels, both from *Miller et al.* [2005], with (c)  $^{39}\text{Ar}$ - $^{40}\text{Ar}$  age groups (grey scale  
 783 bands) defined by pseudo-plateau or plateau ages depicted in this work. (The dotted grey  
 784 curve in (b) is the long term fit of the sea level curve and the straight dotted black segments  
 785 represent the erosion periods; the rectangle and dotted rectangles in (c) represents the  $^{39}\text{Ar}$ -  
 786  $^{40}\text{Ar}$  age groups previously obtained by *Henocque et al.* [1998] and *Colin et al.* [2005],  
 787 respectively; the dark grey histogram in (c) represents the age frequency weighted by the  
 788 error margin for the deposit as a whole; the light grey scale band represents the paroxysm of  
 789 the bauxitic weathering period).

790  
 791 Figure 13. (a) Geomorphological relationships between the lateritic paleolandsurfaces (dotted  
 792 lines) and the sedimentary sequences of the Iullemeden basin of Niger in West Africa (the  
 793 light grey trapezoids represent the denuded bauxites and the vertical black arrow represents  
 794 the total denudation of the regolith. (b) Detailed morphogenetic processes around Tambao  
 795 (black numbers = weathering periods in Ma; grey numbers = erosion periods in Ma; vertical  
 796 grey arrows = regolith denudation and topographic decay).

797



797

798

799

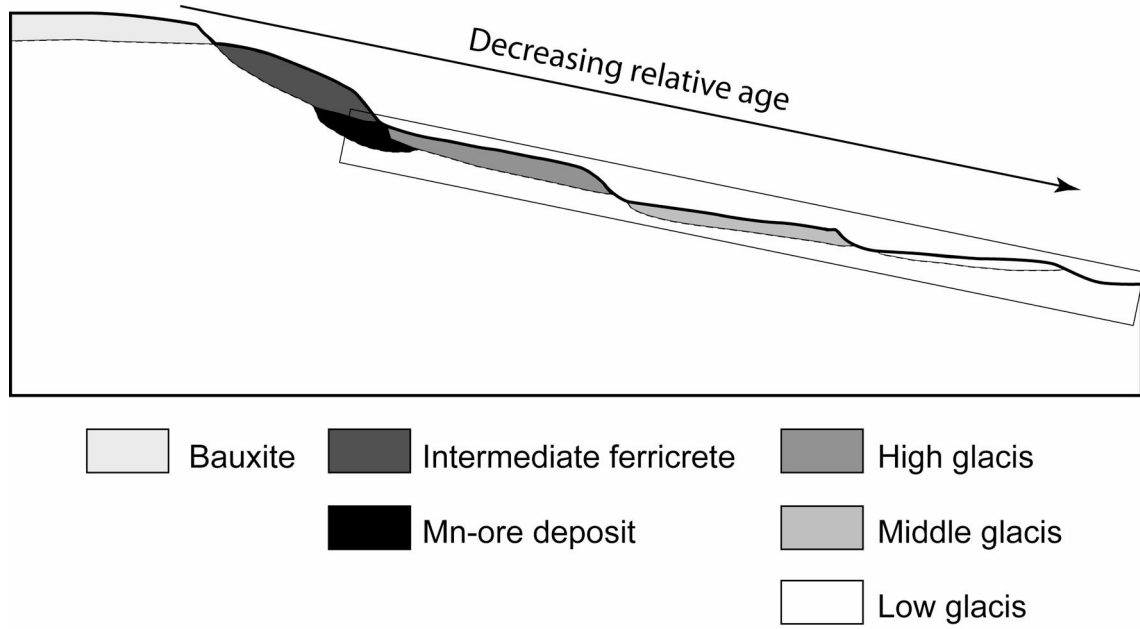


Fig. 1

800

*Beauvais et al., 2008*

801

801

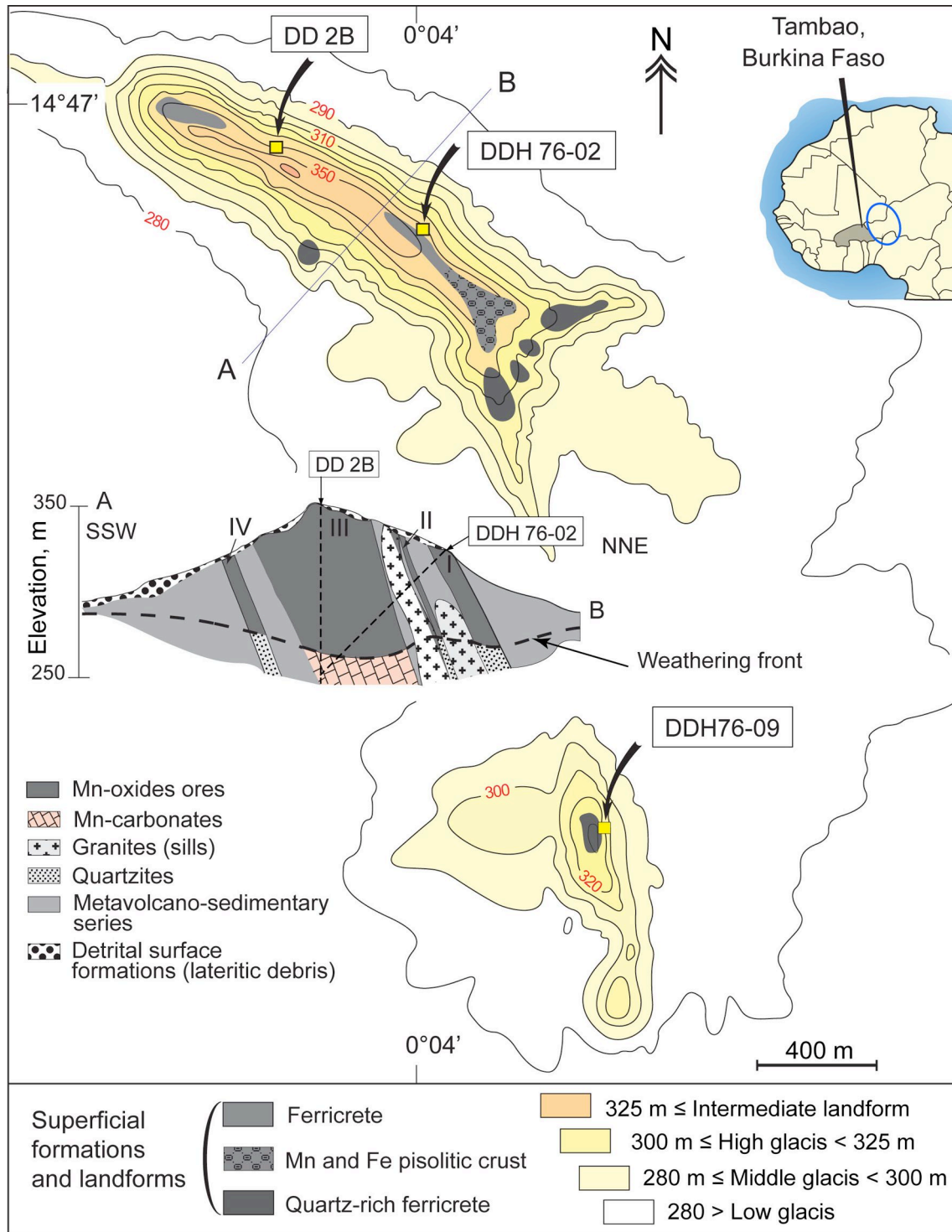


Fig. 2

802

Beauvais et al., 2008

803

803

804

805

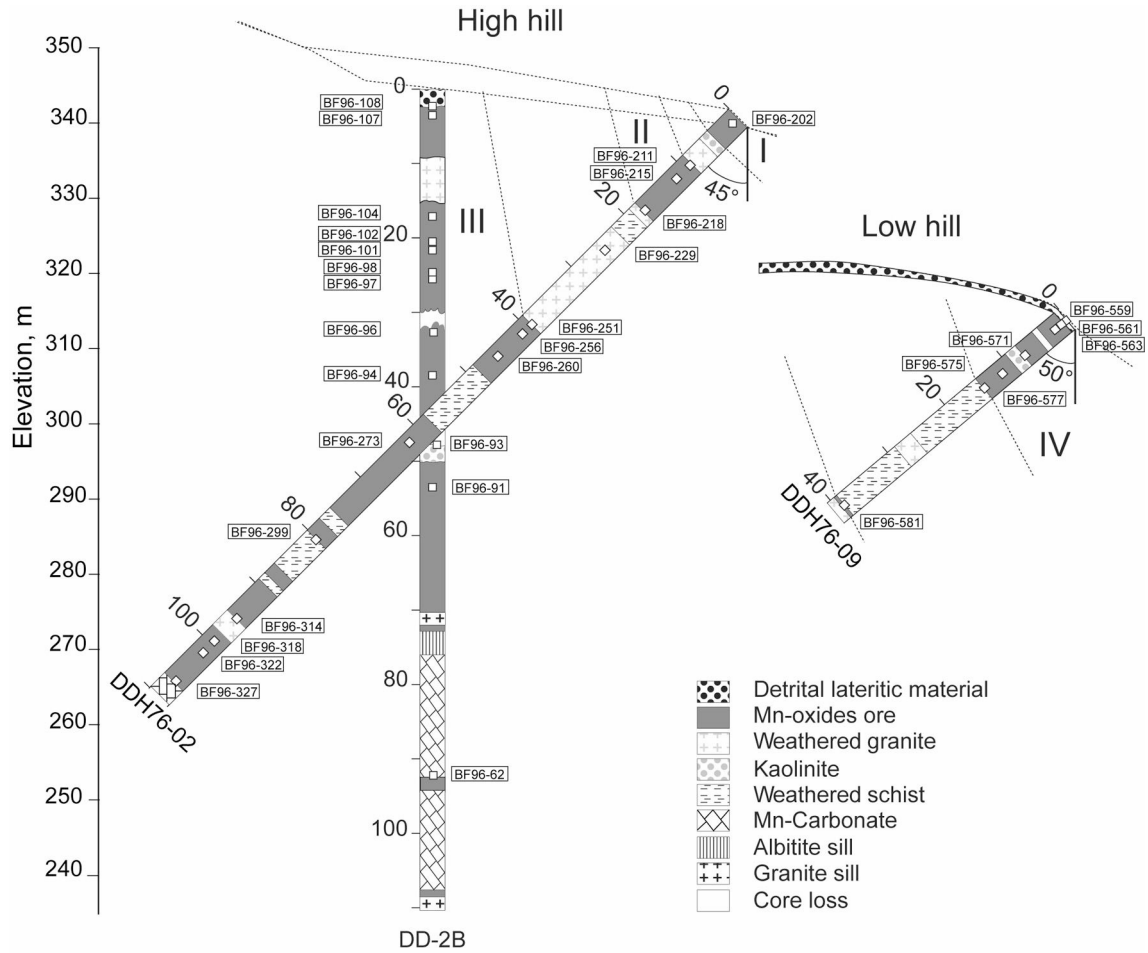


Fig.3

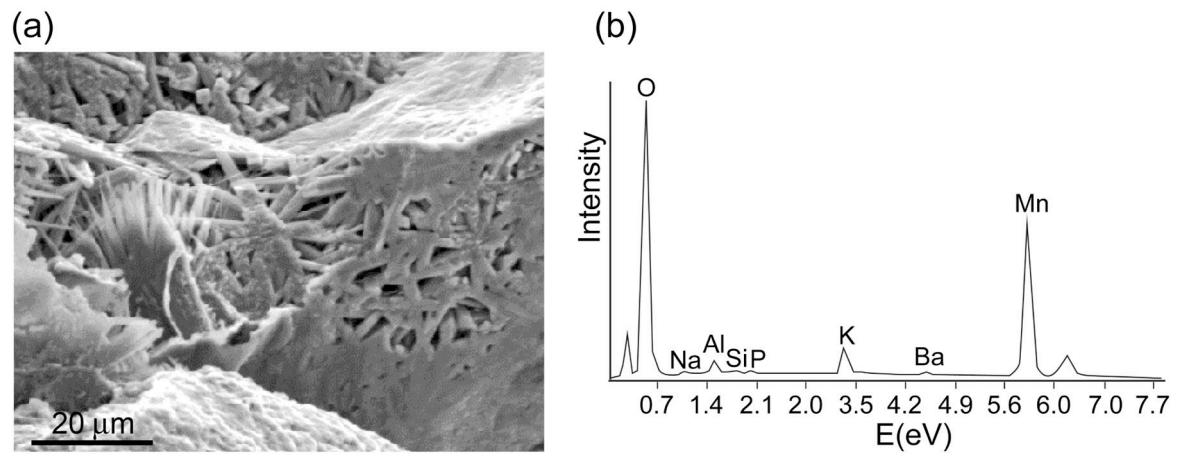
806

Beauvais et al., 2008

807

807

808



809

Fig. 4

*Beauvais et al., 2008*

810

810

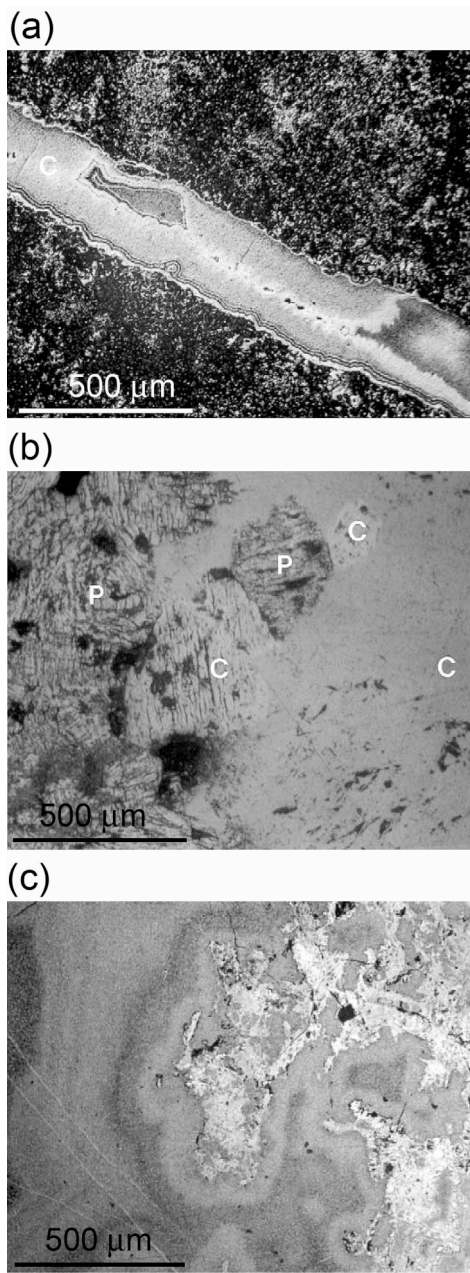


Fig. 5 *Beauvais et al., 2008*

811

812

812

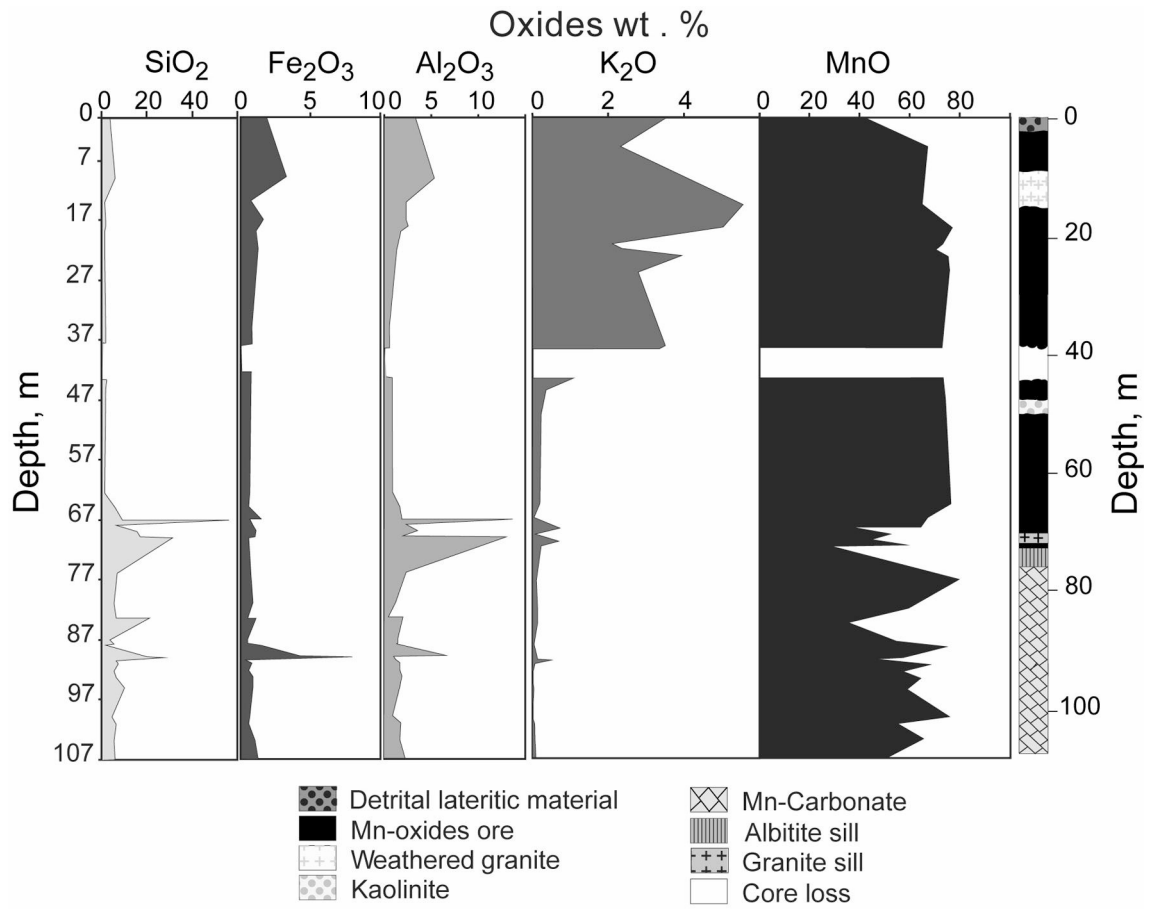


Fig. 6

813

*Beauvais et al., 2008*

814

814

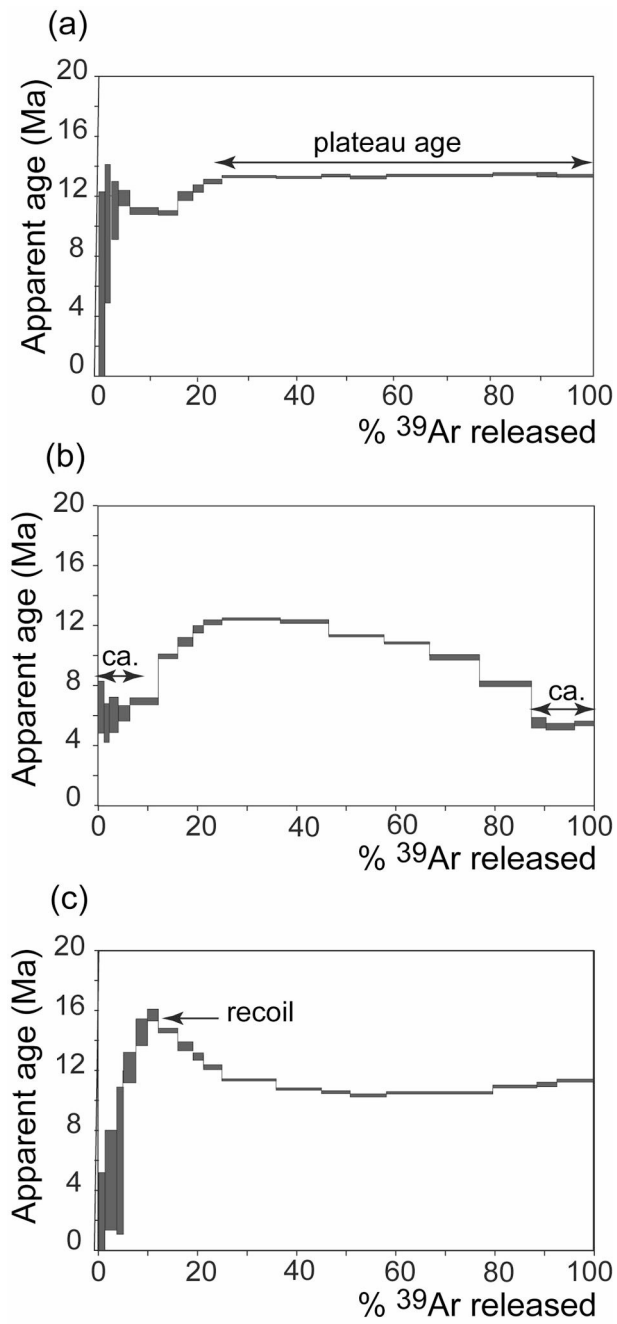


Fig. 7

*Beauvais et al., 2008*

815

816

816

817

818

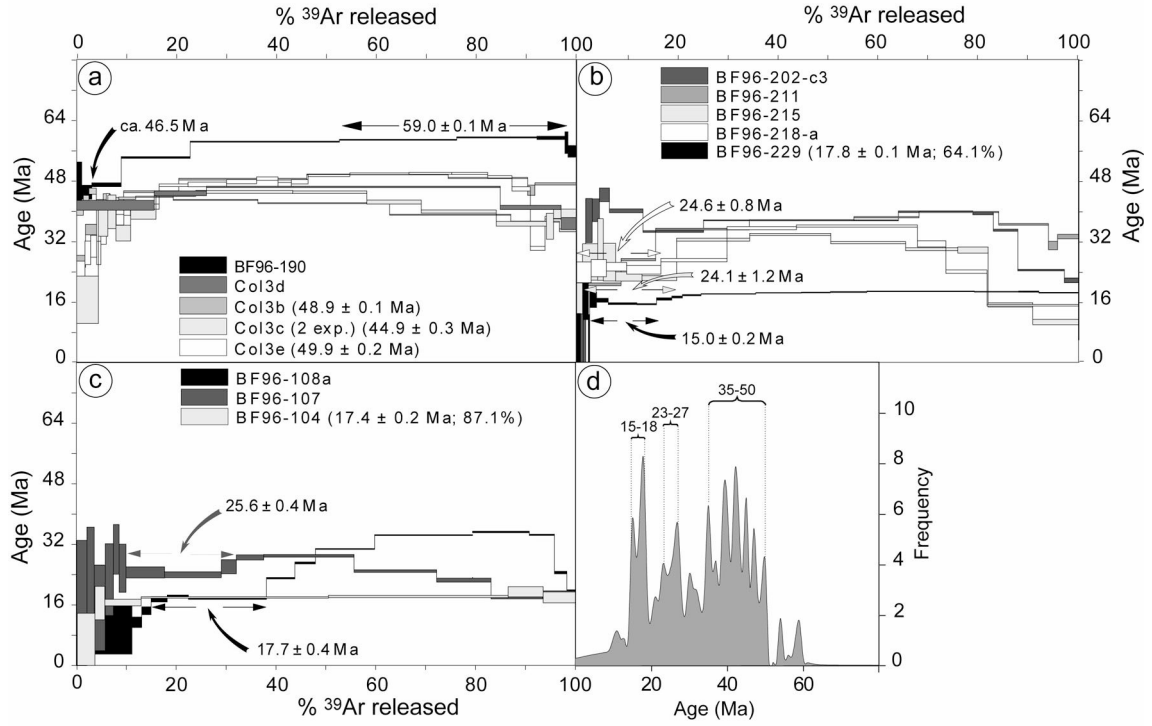


Figure 8

819

Beauvais et al., 2008

820



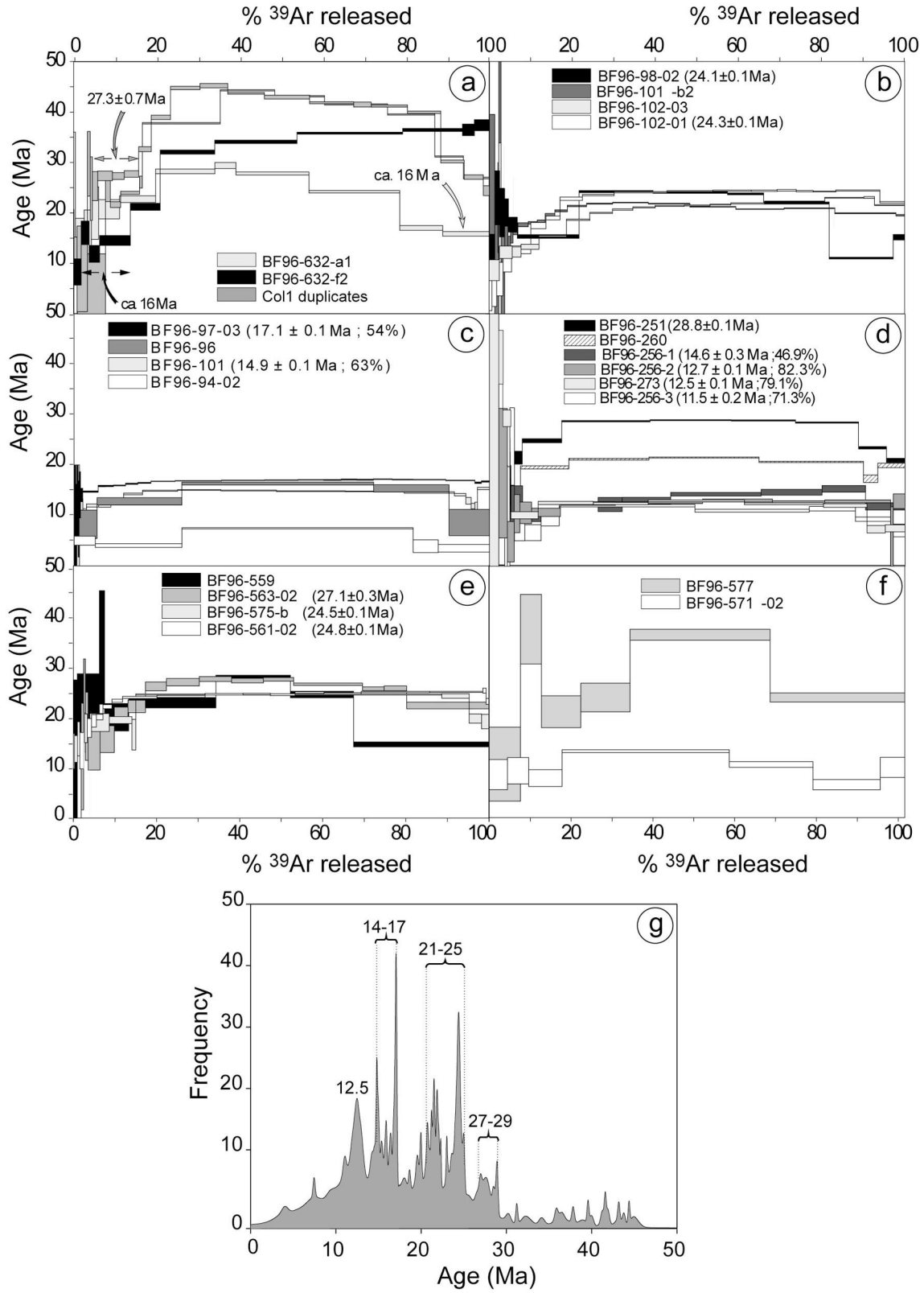


Figure 9

820

Beauvais et al., 2008

821

821

822

823

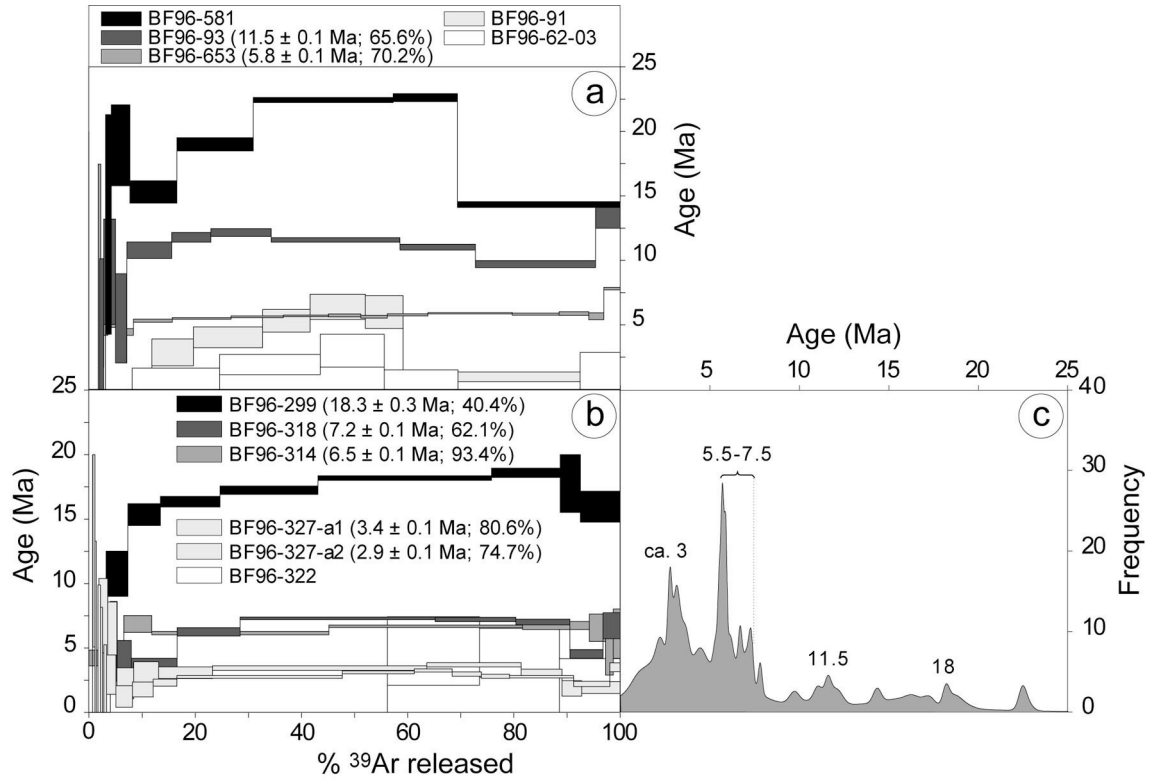


Figure 10

824

*Beauvais et al., 2008*

825

825

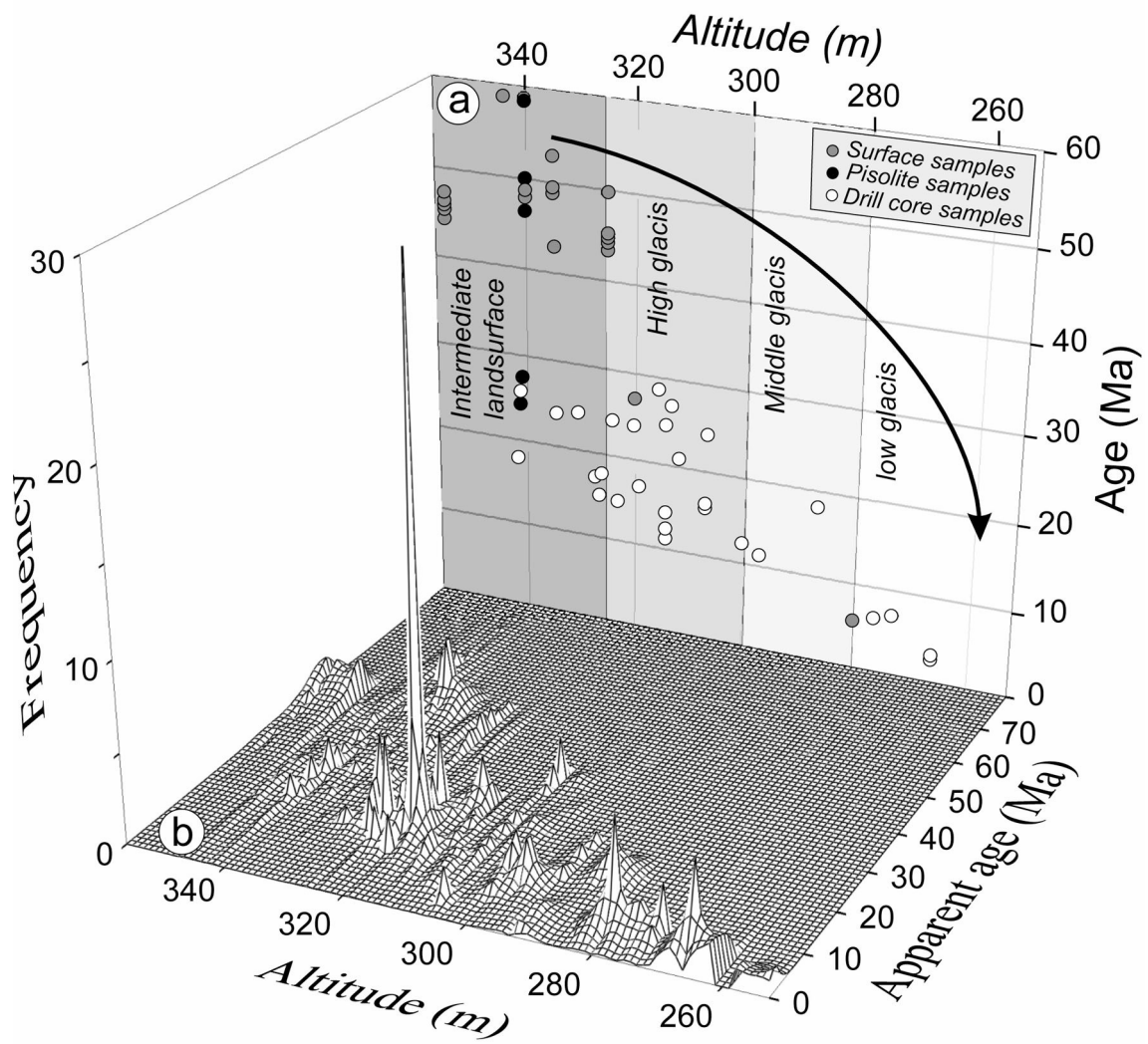


FIG. 11

826

Beauvais et al., 2008

827

827

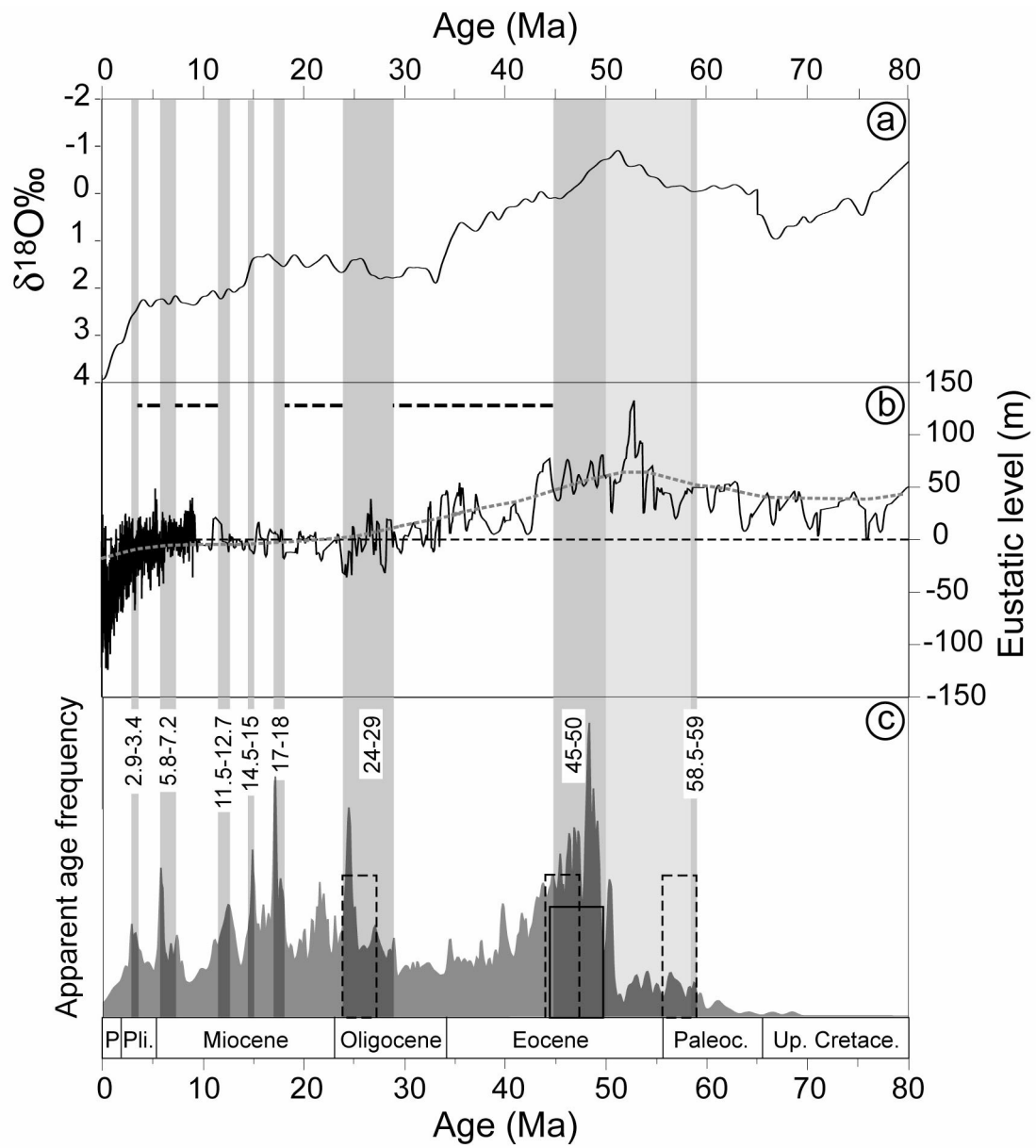


FIG. 12

*Beauvais et al., 2008*

828

829

829

830

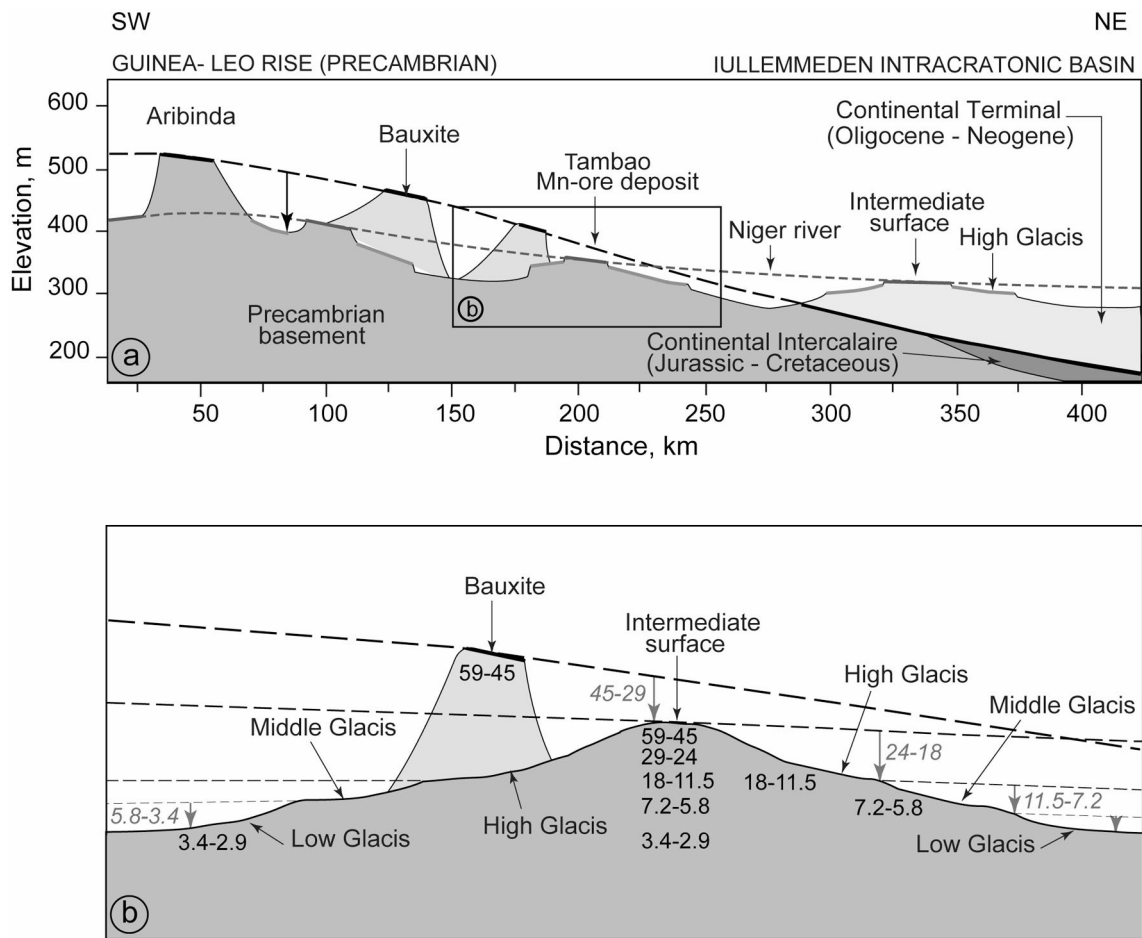


Figure 13

831

Beauvais et al., 2008